A physical analysis of a plasma vacuum seal

Kamycki, Vitto A.S.

Award date:
2020

Department of Applied Physics
Elementary Processes in Gas Discharges Research Group

A Physical Analysis of a Plasma Vacuum Seal

Master thesis

V.A.S. Kamycki

Supervisors:
dr. ir. P.P.M. Blom
dr. ir. J. Beckers

Graduation Committee:
dr. ir. J. Beckers
dr. ir. J. van Dijk
dr. ir. H.C.J. Mulders
dr. ir. R.P.J. Kunnen
dr. ir. P.P.M. Blom

Eindhoven, November, 2020

Abstract

The purpose of this thesis is to understand the principle workings and effectiveness of a plasma vacuum seal. This seal is designed to operate under conditions realistic for a low-pressure wafer handler, where it will attempt to contain nano- and microparticles. This containment is necessary in environments where these small contaminating particles can cause considerable damage, for example in photolithography.

The plasma seal approaches this problem in a peculiar manner. A plasma is generated in a thin gas layer where contaminating particles can flow through. These particles are charged by the plasma, after which an electric field is used to alter the trajectories of the particles. This allows for particle removal without interfering with the flow in the gas layer, which is an important constraint in the forethought objective of the design.

The investigation begins with determining the parameters of the starting point, i.e. the flow and contamination in the gas layer without using the seal. This is done both experimentally and computationally. The experiments were done in an environment that is similar to a real-life application of the so-called SCARA robot arm. Microparticles were injected into a 1.5 mm gap filled with argon at 1200 Pa, with a radially outward flow. After the experiment, the top and bottom plates were removed from the setup and scanned for contaminating particles using a particle counter. The results give information about the properties of the setup and the trajectories of the particles. After this the separate components of the vacuum seal were used to determine the charge properties of the injected particles and the effectiveness of the seal. Combined with the simulations, credible explanations were found for the observed effects. Finally the intended seal design was tested, yielding interesting effects of particle charging in plasma and promising results for the purpose of the seal.

Contents

Chapter 1

Introduction

1.1 Particle Contamination

Upon encountering dust in ones house, most people grimace, take out the vacuum cleaner or dustpan and quickly make sure their home looks neat again. But for what most people consider a minor inconvenience can cause a lot of damage in the wrong places. With ever-growing technological advancements, particle contamination could be one of the most important problems in the production of anything with an integrated circuit in it.

Back in 1965, when integrated computer chips where just being developed, Roger Moore, an R&D worker and future co-founder of Intel, made a prediction about the evolution of integrated circuits. [1] He claimed that the number of transistors on a dense integrated circuit would double every year, later revised to every two years. Considering how little knowledge was available about ICs, it is impressive that his prediction still holds. Over the years the prediction has empirically been dubbed "Moore's Law". Only in recent years the progression of IC's appears to slow down, held back by physical constraints. Nevertheless, progress is not at a standstill, as Samsung claims to be be able to mass produce IC's with a feature size of 3 nm in 2021.

IC production is done by using EUV (extreme ultraviolet) lithography. A laser-induced tin plasma gives off radiation with a wavelength of 13.5 nm, which is directed towards a photoresist covering a thin silicon wafer substrate to etch in extremely precise patterns in a high vacuum. However, with smaller and smaller features come more problems in development. A few specks of dust on a wafer can be enough to make it completely unusable. To that end, a number of options can be considered to avoid problems caused by particles. They can either be removed from the wafer surface after it has been contaminated, or the contamination process can be inhibited. This thesis focuses on the latter, by removing contaminating particles out of the gas flow through the SCARA robot. The SCARA (Selective Compliance Assembly Robot Arm) robot is the main tool for moving around wafers in an EUV lithography machine. These robots are specifically designed for operation under high vacuum. It consists of three independent joints and can move a wafer horizontally to precise locations. Gas is constantly pumped in a thin layer between the joints to avoid friction between the arm parts. Friction would result in sub-optimal movement and unwanted release of aluminum particles from the robot itself. The problem with the gas flow in the joint is that it may contain unwanted hydrocarbon molecules and the aforementioned contaminating particles. Active research is being done in stopping these particles. This thesis focuses on a relatively new idea, a seal for these contaminating particles consisting of a plasma.

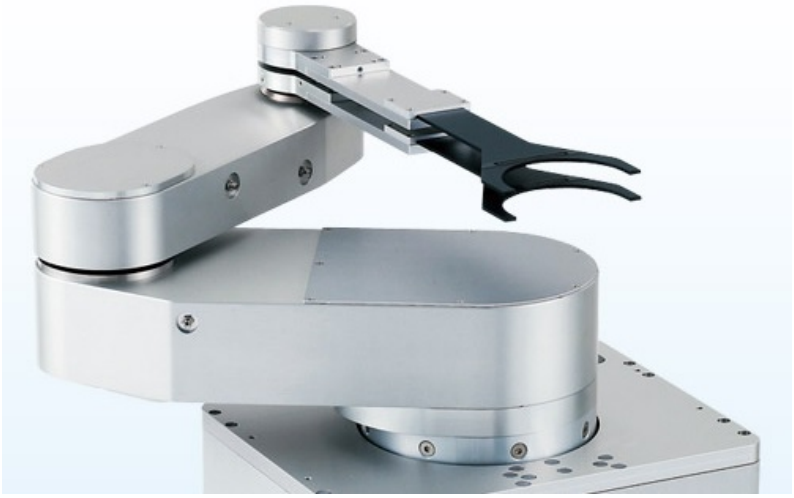

(a) Image of SCARA robot arm. (n.d.) https://www.jel-robot.com/.

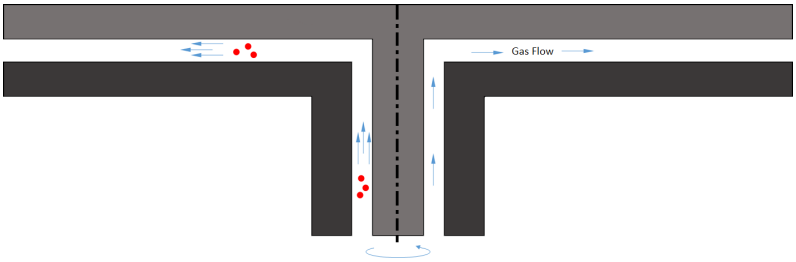

(b) Schematic of a robot arm joint. The different grays represent the 2 different arm parts, which can rotate concentrically around one another. Gas containing contamination flows in the SCARA robot joint gap.

1.2 Plasma (Seal)

Plasma is a fundamental state of matter that makes up over 99 percent of all visible matter in the universe. Despite this fact, it is much less well understood compared to solid, liquid and gas by both scientists and laymen. This is because the circumstances for which a plasma is present are more 'extreme' than those for gasses, liquids and solids. Stable plasmas need a constant power source or a sufficiently high temperature. Almost all plasmas on earth are therefore man-made.

The main property of plasmas is that they contain a large number of high velocity ions and unbound electrons. When an object is placed in a plasma, these charged particles will transfer their charge to the object. In particular this can happen with small dust particles in a plasma. In low concentrations the dust will charge without influencing the plasma. This allows for a relatively easy to understand process where the dust particles gain a charge corresponding to the ion- and electron flux reaching their surface. When particles leave the plasma they retain part of that charge in the plasma afterglow. If an electric field is then applied to the charged particle its path can be manipulated [2]. In the plasma seal to be applied to the SCARA robot this idea is used to keep particles from leaving the confinements of its joint.

(a) The sun (b) Neon signs (c) Laboratory plasma

Figure 1.2: Different types of plasma. (n.d.) https://www.nationalgeographic.org/, https://www.dissolve.com/, https://www.tue.nl/.

1.3 Previous Research

Most of the research relevant to this topic concerns charging of particles in a plasma. In particular their charge in a plasma afterglow. This thesis uses a spatial plasma afterglow, the transition region between the plasma bulk and the gas. While the plasma afterglow is not exactly uncharted territory, the effects of a spatial afterglow have hardly been touched. The combination of a spatial plasma afterglow and plasma particle charging still has a plethora of unanswered questions and interesting qualities. [3], [4] With the relatively new interest in a plasma-based vacuum seal, some studies were recently done in cooperation with VDL-ETG regarding the spatial afterglow. This thesis focuses on obtaining the necessary understanding to design a functional prototype of a plasma vacuum seal. In particular the follow research question was kept in mind:

How are microparticle trajectories and charge influenced by plasma (spatial afterglow) and can plasma be used to create a working particle seal?

1.4 Outline

This thesis is built up as follows:

- Chapter 2 explains the relevant underlying theory regarding the vacuum seal. It focuses on the theory of plasma, particle charging and particle dynamics.
- Chapter 3 describes the experimental setup that was used to research the behaviour of the particles. It also explains how the experimental results are obtained.
- Chapter 4 combines the theory and the setup into a working physical model. This model can be used to explain experimental results as well as computationally optimize the setup.
- Chapter 5 presents the results that were obtained during experimentation. The results are then compared to the physical simulations in order to validate the model.
- Chapter 6 summarizes the conclusions that were drawn from the obtained results.

Chapter 2

Theory

This chapter will present the theoretical background involved in this thesis. First, the basics of plasma and relevant phenomena are explained. Then the contamination processes, particle charging and so-called 'dusty plasma' will be described. Finally, the forces working on plasma embedded particles and their relevance are analyzed.

2.1 Plasma

A plasma, most simply stated, is a partly ionized gas containing neutral gas molecules, as well as ions and unbound electrons. Generation of plasma is achieved by adding energy to a gas, stripping off electrons from the gas molecules. The reactions caused by this energy shift create a variety of species, while the plasma as a whole remains neutral.

A laboratory plasma is generally created by the use of electromagnetic fields. This can be done in a number of ways, though we will focus on capacitively coupled plasmas only. This type of plasma is achieved by applying a potential difference to two electrodes separated by a gas layer. If this voltage is constant over time, Paschen's law dictates the breakdown voltage. This is the voltage at which the plasma transitions to an arc state

$$V_{bd} = \frac{Bpd}{\ln Apd - \ln\ln(1 + \frac{1}{\gamma_{sc}})}. \tag{2.1}$$

Here, A and B are gas constants, while γ_{sc} is the secondary electron emission coefficient, which depends on the electrode material. The pressure is given by p and the electrode distance is given by d. It can be seen that for large pd, the breakdown voltage V_{bd} will increase linearly with pd, while the relation will be exponential for $pd \to 0$. The physical explanation for this is that for low pressure or small electrode distance, there simply are not enough electrons to initiate an electron avalanche. For high pressure or large electrode distance, the electrons are not able to gain high enough energy between two collisions for the appropriate reactions to occur often enough.

One of the most important plasma parameters is the Debye length. Though a plasma as a whole is often electrically neutral, it is full of charged particles. These particle charges are 'shielded' by opposite charges, effectively appearing as neutral from far away. The Debye length is a length-scale over which charge unbalances are shielded by the plasma. The Debye length for charged particles is given by:

$$\lambda_{D_{e,i}} = \sqrt{\frac{\epsilon_0 k_b T_{e,i}}{e^2 n_{e,i}}}. \tag{2.2}$$

Here, $\lambda_{D_{e,i}}$ is the Debye length for electrons and ions respectively, $T_{e,i}$ is the electron/ion temperature, $n_{e,i}$ is the species density and the vacuum permittivity ϵ_0, Boltzmann constant k_b

and elementary charge e represent physical constants. In general, the linearized Debye length given by

$$\lambda_D^{-2} = \lambda_{D_e}^{-2} + \lambda_{D_i}^{-2} \tag{2.3}$$

is often used. In cold plasmas, where $T_e \gg T_i$, the linearized Debye length is roughly equal to the Debye length of the ion species. Using typical values for the parameters of the plasma under investigation here ($T_e = 2$ eV, $T_i = 0.02$ eV, $n_{e,i} \approx 10^{17}$ m^{-3}), a linearized Debye length of ≈ 1 μm is obtained.

The second important length scale is the mean free path. It is defined as the average distance a particle can travel before colliding with another (not necessarily the same) particle. It is given by

$$\lambda_{mfp} = \frac{1}{n\sigma} \tag{2.4}$$

where n is the density of the gas or particles with which the particle collides and σ is the cross section between the two colliding particles.

2.1.1 Plasma Sheath

In a plasma near an interface, a plasma behaves differently than in the bulk. Electrons move a lot faster than other species in a plasma. The thermal velocities of ions and electrons in a plasma are equal to:

$$v_{e,i} = \sqrt{\frac{8k_bT_{e,i}}{\pi m_{e,i}}}.0, \tag{2.5}$$

where $m_{e,i}$ is the species mass. Since $T_e \gtrsim T_i$, electrons are faster by at least a factor $\sqrt{\frac{m_i}{m_e}}$, about a few 100 depending on what ion species are used. This means that electron flux to the wall is initially much larger than the ion flux. The electrons will then be lost to the wall surface. This causes a decay in electron density near the walls, creating a positive space charge. The resulting electric field inside this thin region will point in the direction of the wall, confining electrons in the bulk while accelerating ions towards the wall. The new density distribution near the wall is known as a plasma- or Debye sheath. The thickness of the plasma sheath is typically a few Debye lengths. [5]

2.1.2 RF and AC Driven Plasmas

Things get more complicated when we apply a time varying field between the electrodes. Often an RF-frequency sinusoidal wave is used as the applied voltage waveform. When the applied potential is not constant, Paschen's law for electrical breakdown will not hold due to fundamental changes in plasma properties. An important quantity in these types of plasma is the plasma frequency. Charged particles will follow the time-varying field if their plasma frequency exceeds the frequency of the field. If the plasma frequency is lower than the applied field's frequency, only the average field dictates the particle acceleration. The plasma frequency for electrons and ions is given by the equation:

$$\omega_{e,i} = \sqrt{\frac{n_{e,i}Z_{e,i}^2e^2}{\epsilon_0 m_{e,i}}}. \tag{2.6}$$

Here, $\omega_{e,i}$ is the plasma frequency for electrons or ions, $Z_{e,i}$ is the charge of that species divided by the elementary charge e. For an Ar^+-ion, typical values for the plasma frequency are around 1 MHz, while for electrons this is around 1 GHz. This means that in an RF field, which most

often oscillates at a frequency of 13.56 MHz, only electrons follow the time-varying field, while ions only experience the time-averaged field in the sheath region. In AC generated fields however, with frequencies of approximately 100 kHz or smaller, both electrons and ions can follow the oscillating field. The most important effects are that the average ion temperature will be larger for an AC-plasma and that the mechanism of generating ions changes. [6]

2.1.3 DBD Plasma

A dielectric barrier discharge (or DBD) plasma is a type of capacitively coupled plasma where a dielectric is placed somewhere in the gas layer between the plasma electrodes. There are multiple different geometries for DBD setups. The one used in this thesis is the case of a dielectric attached to a high voltage AC electrode, and a grounded electrode without a dielectric barrier as shown in the figure below.

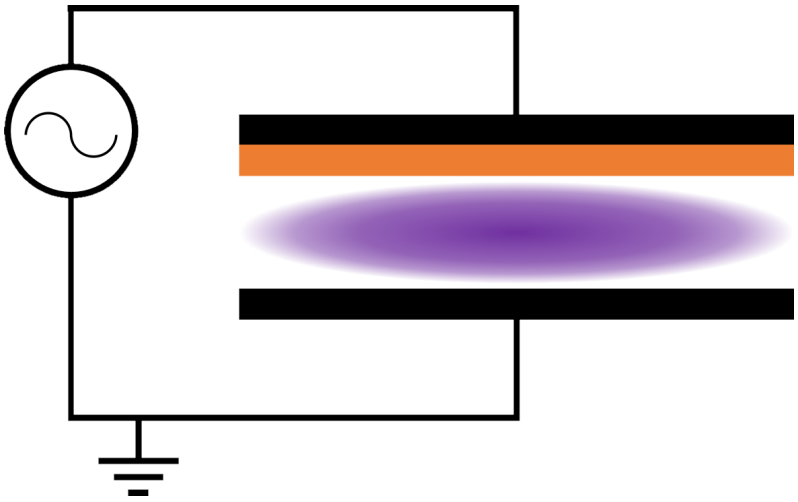

Figure 2.1: Schematic drawing of a volume DBD circuit. Orange represents a dielectric while purple represents a plasma.

As will be explained in chapter 3, a planar volume DBD is used. The primary reason for the use of such DBD is that it is the most accurate representation of the practical idea for the plasma seal. It is also a relatively easy setup to create and control. Dielectric barrier discharges are regularly used in atmospheric pressure for its electrohydrodynamic properties and ozone generation. Its discharge used to be considered as always filamentary [7]. However, for example in lower pressure regimes, the discharge can be diffuse as was shown by Wagenaars et al. [8]. The discharge is mostly identical to the regular Townsend mechanism of a low pressure glow. The difference lies in the capacitive properties of the dielectric. The residual charge on the dielectric can assist or partly counteract the electrodes depending on the stage in the RF cycle. This has a number of advantages including the inhibition of thermal plasma or spark generation.

2.1.4 Plasma Afterglow

The main mechanisms of a capacitively coupled plasma have now been explained in the case of a purely 1-dimensional plasma. Unfortunately a physical example of this does not exist. There are boundary effects present perpendicular to the electrodes and the plasma-gas transition is not infinitely sharp. The gradual depletion of plasma is known as a plasma afterglow. The first publication showing a plasma afterglow was released in 1953 by Schmeltekopf and Broida [9]. After external plasma generation was switched off, the plasma remained visible for a short period of time, hence the name afterglow. This type of afterglow is known as a temporal afterglow. A spatial afterglow refers to the gradual plasma depletion at the edges of the working volume where

no net ionization occurs. The phenomenon is caused by species in the area where though they are not energized directly, while they still have more energy than they would have had in the gaseous state. The particles then lose their energy by collisions with other particles in the same manner as in the main plasma. In a temporal afterglow, this continues until the plasma fizzles out before thermal equilibrium with the gas is reached. In a spatial afterglow the plasma encompasses a larger area than just in between the electrodes, with lower density and temperature.

Electron Temperature Relaxation

The decay of the electron temperature, which is typically a few eV in the active plasma region, happens faster in the aftergloe region than the decay of the ion temperature. The normalised electron temperature $\tilde{T} = T_e/T_i$ is therefore introduced to describe the system. The relaxation of this temperature is described by the following differential equation. [10]

$$\frac{d\tilde{T}}{dt} = -(\tilde{T} - 1)/\tau_T. \tag{2.7}$$

Here, τ_T is the timescale relevant to the temperature relaxation given by

$$\tau_T = \sqrt{\frac{2m_i}{\pi m_e \tilde{T}}} \frac{\lambda_{mfp}}{v_{th,i}} = \frac{\tau_T^\infty}{\sqrt{\tilde{T}}}, \tag{2.8}$$

where λ_{mfp} is the electron mean free path and $v_{th,i}$ the thermal ion velocity. Note that the electron mean free path depends on the electron-neutral cross section which also depends on the electron temperature.

Plasma Density Decay

As like the electron temperature, the plasma density will decay away from the main plasma bulk. This is due to volume recombination between species as well as (ambipolar) diffusion to the walls. The first component is very small at low pressure and a thin gas layer [11]. The plasma density decay is therefore governed by diffusion to the walls and respective recombination, and can be described by the following differential equation

$$\frac{d\tilde{n}}{dt} = \frac{\tilde{n}}{\tau_D} \tag{2.9}$$

where $\tilde{n}$ is the relative species density with respect to the initial density $\frac{n_{i,e}}{n_{i0,e0}}$. τ_D is the timescale for diffusion to the wall given by

$$\tau_D = \frac{\Lambda^2}{D_a} \simeq \frac{3\Lambda^2}{\lambda_{mfp,i} v_{th,i}} \frac{1}{1+\tilde{T}} = \frac{2}{1+\tilde{T}} \tau_n^\infty \tag{2.10}$$

with Λ the characteristic diffusion length and D_a the ambipolar diffusion constant. Note that the plasma decay is coupled to the electron temperature relaxation.

Quasi-neutrality breakdown

The last effect of the plasma afterglow is the breakdown of quasi-neutrality. At some point in the afteglow, the Debye length will have increased to be comparable to the diffusion length of the system Λ. At this point the electrons and ions will be able to diffuse independently. The species density is then equal to

$$n_{qn} = \frac{\epsilon_0 k_b T}{e^2 \Lambda^2} \approx 10^9 m^{-3}. \tag{2.11}$$

Note that there is no subscript for the temperature T, as the ions and electrons are in equilibrium with the gas in this stage. The quasi-neutrality breakdown in a temporal afterglow occurs at

$$\tau_{qn} \approx \ln(n_{qn}) \tau_D^\infty. \tag{2.12}$$

At this point, the electron density will decrease faster than the ion density because of the higher mobility. This will create a net positive space charge.

2.2 Complex Plasma

Up until now, the plasma theory assumes a perfectly 'clean' plasma without any foreign species. In the experiments for this thesis, particles are injected into a plasma. When small ($< 1mm$) particles are part of the overall balance in a plasma, it is called a complex (or dusty) plasma. This section describes what happens to both the particles as well as the plasma as a whole.

2.2.1 Particle charging

When a particle enters a plasma, it will have collisions with charged particles. Essentially particles larger than $\approx 10 - 20$ nm can be viewed as floating walls. It is known that in general a floating wall will obtain a negative charge due to the higher thermal velocity of electrons. Larger particles will therefore be charged negatively, repelling electrons and attracting ions until an equilibrium is reached. The resulting balance will fluctuate due to the collisions being stochastic in nature. Some particles are able to charge positively due to secondary electron emission and photo-ionization, but the particles used in this thesis are of μm scale in which the electron- and ion flux theory applies. The different particle charging mechanisms will be described in the following paragraphs.

Collection of charge carriers
Charged species that collide with the particle can be collected at the particle surface. Initially, primarily electrons will be colliding with the particle because of their much higher mobility. At small distances from the particle an electric field will be generated, which is shielded completely after a few Debye lengths. In this field additional electrons ill be repelled while positive ions are accelerated to the particle surface. Eventually an equilibrium between the electron and ion flux is reached. This is the main mechanism of particle charging for μm sized particles under normal plasma conditions.

Secondary electron emission
High energy electrons and ions that impact on a particle can release electrons from the surface due to the ionization. The number of released electrons is called the secondary electron yield. The secondary electron yield is dictated by the energy of the impacting charged particles and the work function of the particle. The work function is surface dependent and can vary from particle to particle. For pure bulk material it is equal to a few eV. It is therefore likely that secondary electron emission occurs.

Thermionic emission
Thermionic emission can occur when the thermal energy of a particle exceeds its work function. Charge carriers are then emitted from the surface. For this process to occur the particles need to be heated significantly by the plasma. This is unlikely because of the relatively low ion temperature and transit time.

Field emission
Field emission is the emission of electrons in an electric field. A high field can pull electrons from a surface, decharging it in the process. This process scales with total charge on the surface, effectively limiting the maximum particle charge in an electric field.

2.2.2 OML Theory

Orbital motion limited (OML) theory is the main theory for describing particle charging in dusty plasma [12]. It assumes a small particle radius compared to the Debye length and is not applicable in every situation, hence the 'limited'. As far as theory for particle charging in a complex plasma goes, it is relatively easy to obtain useful and satisfactory results [13]. The main idea is to compare ion and electron currents in a collisionless plasma. [14] The OML theory derivation starts with

the radial electron density distribution around a particle.

$$n_e(r) = n_e \exp\left(\frac{eV(r)}{k_b T_e}\right) \tag{2.13}$$

with $V(r)$ the potential distribution of the charged particle. This Boltzmann distribution assumes no external forces on electrons and thermal equilibrium. This is not always the case but for OML theory these assumptions are sufficient for a physical result. The electron current is then equal to

$$I_e = -4\pi r_p^2 e n_e(r) \frac{v_{th,e}}{4} = -\pi r_p^2 e n_e \sqrt{\frac{8k_b T_e}{\pi m_e}} \exp\left(\frac{eV(r)}{k_b T_e}\right). \tag{2.14}$$

For ions, a Maxwellian distribution is used. The ion current was derived by Laframboise [15] to be

$$I_i = \pi r_p^2 e n_i \sqrt{\frac{8k_b T_i}{\pi m_i}} \left(1 - \frac{eV(r)}{k_b T_i}\right). \tag{2.15}$$

assuming only singularly charged positive ions. The equilibrium $-I_e = I_i$ at $r = r_p$ can then be written as

$$\frac{n_e}{n_i} \exp\left(\frac{eV(r_p)}{k_b T_e}\right) = \sqrt{\frac{T_i m_e}{T_e m_i}} \left(1 - \frac{eV(r_p)}{k_b T_i}\right). \tag{2.16}$$

Filling in this equation with the plasma parameters gives an expression for the surface potential of the particle. When considering the particle to be a perfect capacitor with capacitance

$$C_p = 4\pi\epsilon_0 r_p \tag{2.17}$$

the particle charge can be calculated using

$$Q_p = C_p V(r_p) = 4\pi\epsilon_0 r_p V(r_p). \tag{2.18}$$

Using comparable values for the parameters used in this thesis (see 2.2 and using argon) an equilibrium charge of approximately $7 * 10^3$ elementary charges is obtained. However, it has been shown that the equilibrium charge can be much lower for higher pressures. As the experiments were done at a pressure of 1200 Pa, it is assumed, based on the results of Ratsynkaia et al. [16], that the particle charge will be at least 10 times lower than the value according to OML theory. As different particles vary in size in the experiments and the electron temperature is not precisely known, the equilibrium charge dependence according to OML theory is shown in figure 2.2 below.

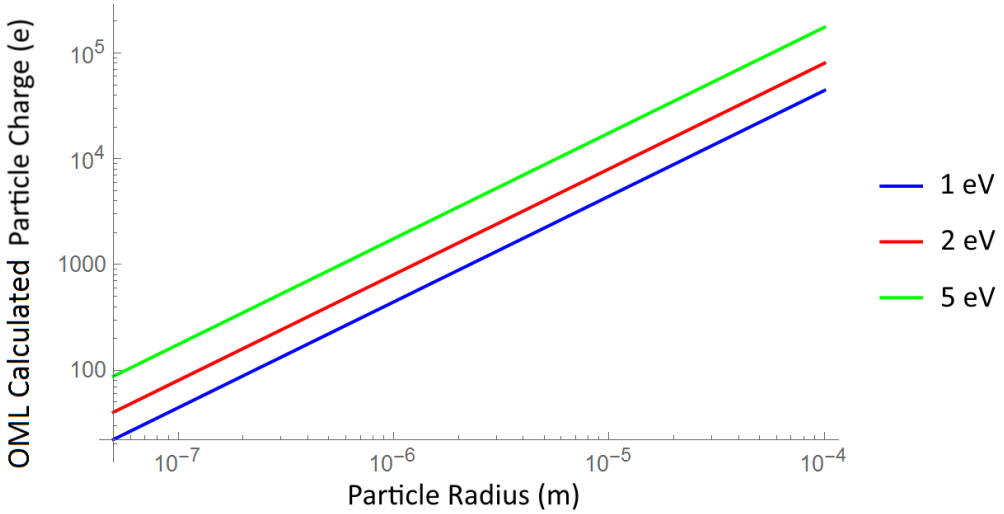

Figure 2.2: Graph of equilibrium charge on a particle according to OML theory versus the particle radius. The different lines represent different electron temperatures. The graph assumes argon and an ion temperature equal to room temperature. $\frac{n_e}{n_i} = 1$,$T_e = 2$ eV,$T_i = 300$ K, $r_p = 2.5$ μm

Note that the OML theory is a first order approximation in calculating the equilibrium dust charge. First of all, only the collection of charge carriers is used. Although this is the main source of particle charge, this does not paint the whole picture. The OML theory also uses a lot of assumptions. The particle radius should be much smaller than the Debye length and the Debye length should be much smaller than the mean free path to ensure a collisionless plasma. It also assumes that all particles below a certain impact parameter are caught. Finally it should be noted that the equilibrium charge is not necessarily the final charge on a particle after exposing it to a plasma. Random fluctuations influence the charge constantly with each charged species impact. The particle decharges in the afterglow and outside of the plasma bulk. Furthermore, the time a particle spends in a plasma might not be long enough for the calculated equilibrium to be reached. These last shortcomings with the general OML theory will be explained in the next few subsections.

2.2.3 Charge fluctuations

When a particle has reached its equilibrium charge, charged species do not stop impinging on it, the charge on a particle will still continue to vary. [17] Since these collisions are stochastic, a bit of statistic will come into play for determining the charge variations. The equilibrium charge in the active plasma region will still be several orders of magnitude larger than these variations, meaning they mainly come into play when a particle leaves the plasma. Matsoukas and Russel [18] have shown that the statistical distribution of charge on a particle is approximately Gaussian for a particle if $\frac{e^2}{4\pi\epsilon_0 r_p} << k_b T_e$. In general this holds for micrometer-sized particles. The Gaussian distribution then is given by

$$f(Z) = \frac{1}{\sigma\sqrt{2\pi}} \exp\left(-\frac{(Z - Z_D)^2}{2\sigma^2}\right) \tag{2.19}$$

with Z_D the average charge on a particle divided by the elementary charge and σ the standard deviation, derived using OML theory to be

$$\sigma^2 = \frac{1}{\beta_e}\left(\frac{1 - \tilde{T}\beta_e Z_D}{\tilde{T} + 1 - \tilde{T}\beta_e Z_D}\right) \tag{2.20}$$

2.2.4 Charging time

So far the assumption was held that particles in a plasma instantly achieve their equilibrium charge, this is of course not true. This subsection will derive an expression for the time a particle needs to charge to its equilibrium value. This knowledge is needed for determining how effective a plasma is in charging a particle as well as how a setup or application should be designed around this.

The charging process as described by the OML theory, yields the following expression for the time-dependent charge of a particle:

$$\frac{dQ_p}{dt} = I_e + I_i = -\pi r_p^2 e\sqrt{\frac{8k_b}{\pi}}\left(n_e\sqrt{\frac{T_e}{m_e}}\exp\left(\frac{eV(r)}{k_b T_e}\right) - n_i\sqrt{\frac{T_i}{m_i}}\left(1 - \frac{eV(r)}{k_b T_i}\right)\right) \tag{2.21}$$

In equilibrium, this can be equated to zero, eventually leading to

$$1 - + \tilde{T}y - \frac{v_{th,e}}{v_{th,i}}\exp(-y) = 0 \tag{2.22}$$

with $y = \frac{eV(r)}{k_b T_e}$. The charging time can be estimated using [19]

$$\tau_c = \alpha / \left|\frac{d\alpha}{dt}\right|. \tag{2.23}$$

Here, α is a small perturbation around $\tilde{y}$, the equilibrium value of y. Now $\tilde{y}+\alpha$ is substituted for y in equation 2.19 using equation 2.20. After some derivation, this leads to a charging time of

$$\tau_c = \frac{\epsilon_0}{e^2 r_p n_{i,e}} \sqrt{2\pi k_b T_i m_i e^2} \frac{1}{1+\tilde{y}}. \tag{2.24}$$

After substituting the aforementioned typical values for the parameters, the maximum typical charging time for the particles used in this thesis is calculated to be equal to 10 μs. Assuming a particle velocity equal to the flow velocity in the plasma (≈ 0.2m/s) and an electrode width of 10 mm, the particle transit time through the plasma is equal to 50 ms. This means that the particles will obtain their equilibrium charge when travelling through the plasma.

2.2.5 Particles in afterglow

After a particle has been charged in the plasma bulk, it enters a spatial afterglow. The regions of the afterglow and the effect on the particle equilibrium charge is explained in this section using figure 2.3.

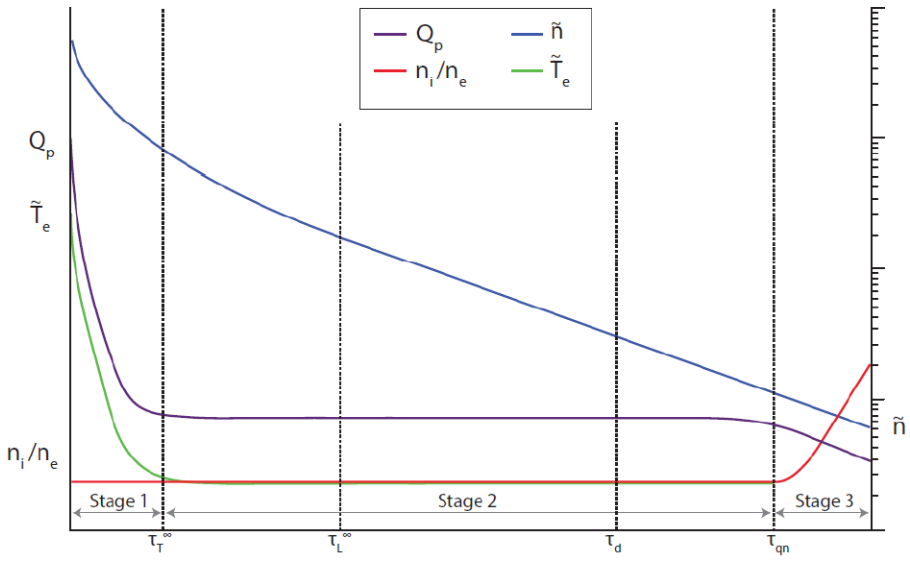

Figure 2.3: Temporal evolution of plasma parameters and dust charge in a plasma afterglow.

Once entering a spatial plasma afterglow, the particle will then quickly start to decharge in the first region because of a drop in electron temperature. When the electron temperature has dropped to the ambient temperature, a new, lower charge equilibrium exists. This is not necessarily the exact charge of the particle in this region, because the particle might leave this stage of the afterglow before it has decharged to its new equilibrium value. The drop in plasma density has little effect on the particle charge, assuming quasi-neutrality still holds. [20] When the final region where ions and electrons diffuse independently is reached, the particle will again decharge or even charge positively [21]. Depending on the particle and the setup, the effects of the afterglow can be both inconvenient or helpful.

2.3 Forces on Particles

The forces that act on the contaminating particles must be explored in order to explain the results of the experiments. Knowing these forces is also critical in creating a simulation to prove the accuracy of the experiments and their interpretations. All relevant forces are laid out and explained in the upcoming subsections.

2.3.1 Gravity

The gravitational force acts constantly on all particles in the system. The force F_{grav} is equal to

$$\vec{F}_{grav} = \frac{4}{3}\pi r^3 \rho_p g \tag{2.25}$$

Where r is the radius of the spherical particles, ρ_p is the density of the particles and g is the gravitational acceleration on earth ≈ 9.81 m/s^2. For a glass particle with a radius of 5 μm, $\vec{F}_{grav}$ is equal to 12.8 pN.

2.3.2 Neutral Drag Force

Neutral drag force is a result of the microparticle colliding with gas particles in a flow, transferring momentum. This force is always opposite to the velocity of the particle with respect to the gas. In order to know what type of drag force is applicable, the Reynolds number of the gas flow and the Knudsen number of the particles must be known. They are respectively given by:

$$Re = \frac{\rho_g u D}{\mu} \qquad Kn = \frac{\lambda_{mfp}}{r} \tag{2.26}$$

In the first equation, $\rho_g = 1.784$ kg/m^3 is equal to the density of the gas, here argon, $u \approx 0.3$ m/s represents the typical velocity of the flow, $D = 1.5$ mm is the length scale of the system and μ is the dynamic viscosity of the gas, for argon this is equal to $2.23 * 10^{-5}$ Pa s. In the second equation, λ_{mfp} is the mean free path of the neutral gas species, for argon this is equal to 5.495 μm. For these inputs, $Re = 36$ and $Kn \approx 1$. This means that since $Re < 2300$ the flow is clearly laminar.

The Knudsen number can be seen here as a scale for whether the drag is hydrodynamic ($Kn \ll 1$) or kinetic ($Kn \gg 1$). Since the calculated Knudsen number is about equal to unity and the used particles are of varying size, both drag types are worth looking at. The hydrodynamic drag can simply be calculated using Stokes' law:

$$\vec{F}_D = 6\pi r \mu (\vec{v}_N - \vec{v}_p) \tag{2.27}$$

This scales linearly with the velocity v_p of the particle relative to the velocity of the neutrals v_N. [22]

For medium Knudsen numbers ($10^{-3} < Kn < 10$) Stokes' law no longer holds. The no-slip condition is no longer valid and it is an important assumption for deriving Stokes' law. A correction is needed, which is known as the Cunningham slip correction. After some derivation the new drag force is given by:

$$\vec{F}_D = \frac{\rho_g C_d A |v_p|}{2C_c}(\vec{v}_N - \vec{v}_p) \tag{2.28}$$

Here, C_d is the drag coefficient, A is the cross-sectional area of the particle, and C_c is the Cunningham correction factor equal to:

$$C_c = 1 + Kn(\alpha + \beta \exp(-\frac{\gamma}{Kn})) \tag{2.29}$$

where α, β and γ are empirically determined constants depending on the particle and the fluid.

When the kinematic regime is entered, the drag force is calculated in one of two ways. This depends on the ratio between the relative velocity of the particle with respect to the flow velocity and the thermal velocity of the neutral species $\frac{v_N - v_p}{v_{th}}$ When this ratio is small ($\ll 1$), The Epstein relation follows [23]:

$$\vec{F}_D = \frac{8}{3}\sqrt{2\pi} r^2 m_N n_N v_{th}(\vec{v}_N - \vec{v}_p) \tag{2.30}$$

for specular reflection of the incoming gas particles from the particle's surface and

$$\vec{F}_D = \frac{8}{3}\sqrt{2\pi} r^2 m_N n_N v_{th}(1 + \frac{\pi}{8})(\vec{v}_N - \vec{v}_p) \tag{2.31}$$

for perfectly diffuse reflection. Here, m_N and n_N are the mass and number density of the gas particles. These relations were empirically shown by Zhigang and Wang [24] to result in an average drag force of:

$$\vec{F}_D = \frac{6\pi\mu r^2}{\lambda_{mfp}(A + B)}(\vec{v}_N - \vec{v}_p) \tag{2.32}$$

The parameters A and B depend on the gas type and temperature, for the gas used in this thesis, their sum is approximately equal to 1.7.

When the ratio $\frac{v_N - v_p}{v_{th}}$ is large ($\gg 1$) the drag force is given by: [25]

$$\vec{F}_D = \pi r^2 m_N n_N |v_N - v_p|(\vec{v}_N - \vec{v}_p) \tag{2.33}$$

In this thesis and in most laboratory experiments $\frac{v_N - v_p}{v_{th}} \ll 1$ and relation 2.32 should be used for these types of flow.

2.3.3 Electric Force

The electric force applies to the charged particles in the system. It is one of the major forces in the experiments, as it is the main driving force for the vacuum seal. The electric force is given by:

$$\vec{F}_E = Q\vec{E} \tag{2.34}$$

where Q is the charge on the particle and $\vec{E}$ is the local electric field, either plasma self-induced or externally applied. Positive charges move in the direction of the field vector while negative charges move in the opposite direction of the field.

In the framework of this thesis the main source of the electric field will be the electrodes of the setup, though particles can also be affected by the fields of other particles. The Coulomb force between two spherical charged objects in a vacuum is given by:

$$\vec{F}_E = \frac{Q_1 Q_2}{4\pi\epsilon_0 |d|^2}\hat{d} \tag{2.35}$$

Where Q_1 and Q_2 are the charges of particle 1 and particle 2 respectively, ϵ_0 is the vacuum permittivity, $|d|$ is the absolute numerical value of the distance between the particles and $\hat{d}$ is the unit vector pointing from one particle to the other.

Unfortunately, this equation does not hold in the experiments as Debye shielding takes place. This means the effective charge has to be used for determining the Coulomb interaction. This is given by:

$$Q_{eff} = Q \exp\left(-\frac{d}{\lambda_D}\right) \tag{2.36}$$

However, this is still not complete, as this assumes a constant plasma bulk. To account for the plasma sheath and the afterglow, the Debye length needs to be looked at. It was suggested by Land en Goedheer [26] to use the linearized Debye length (Equation 2.3) and use a correction term for the ion Debye length to factor in the ion velocity in the sheath:

$$\lambda_{D_i,eff}^2 = \lambda_{D_i}^2 v_{i,th} \left(1 + \frac{u_i^2}{v_{i,th}^2}\right) \tag{2.37}$$

with $v_{i,th}$ the thermal ion velocity and λ_{D_i} the ion Debye length 2.2. Keeping this in mind it should be noted that the mutual Coulomb interaction is very small if particles are not close together. It can be assumed to be negligible if $n_{dust} \ll 1/\lambda_D^3$.

2.3.4 Ion Drag Force

The ion drag force is caused by ions acting on charged dust particles. Ions can have a non-random velocity due to electric fields in the setup. Their momentum can be transferred to the dust particle, effectively creating a drag force opposite to the relative velocity of the dust particle. Due to Coulomb interaction, the effective cross section of these collisions is higher than the normal geometrical cross section of πr^2. The ion drag force consists of two components with different mechanisms.

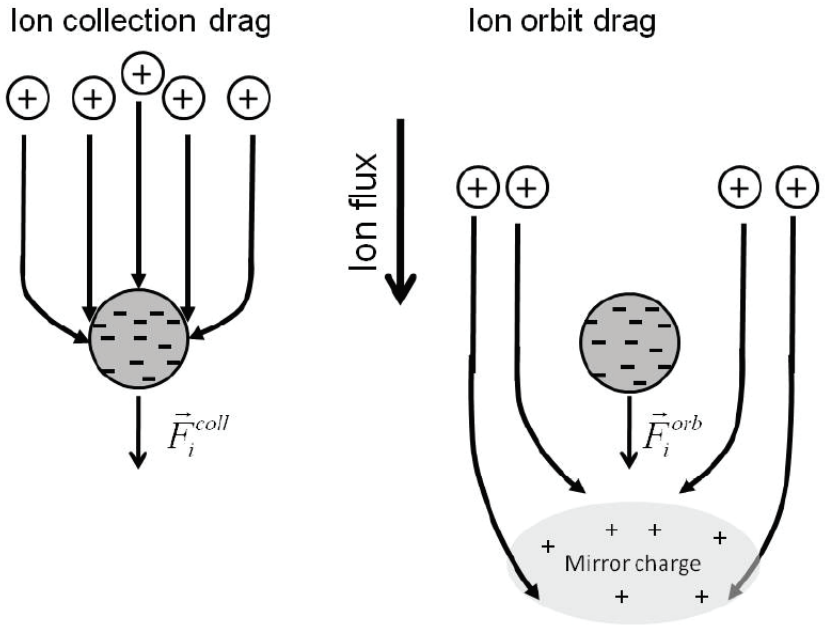

Figure 2.4: Schematic drawing of the effects of the two ion drag force components. From [27].

The first component is the ion collection drag force. It is caused by direct ion collisions with the particle described by the expanded cross section caused by Coulomb interaction. Note that because the ions are physically collected by the dust particle, its total charge will decrease. The ion collection drag force is given by

$$\vec{F}_{i,coll} = \pi r^2 n_i m_i u_i \vec{u}_i (1 - \frac{2eV(r_p)}{m_i u_i^2}) \tag{2.38}$$

where u_i is the non-random ion velocity caused by an electric field and $V(r_p)$ is the surface potential of the dust particle as a function of its radius. [28]

The second component of the ion drag force is the orbit ion drag force. This is an indirect momentum transfer as there are no physical collisions. The force is caused by the deflection of ions, again because of Coulomb interactions. The deflection creates an attractive mirror charge behind the dust particle. The orbit ion drag force was calculated by Thomas et al. [29] to be

$$\vec{F}_E = \vec{F}_{i,coll} = 4\pi n_i m_i u_i \vec{u}_i b_{\pi/2}^2 \Gamma \tag{2.39}$$

with $b_{\pi/2}$ the impact parameter of $r\frac{-eV_0}{m_i u_i^2}$ with V_0 the particle potential and Γ the Coulomb logarithm given by

$$\Gamma = \ln\left(\frac{\lambda_s + b_{\pi/2}}{r + b_{\pi/2}}\right) \tag{2.40}$$

with

$$\lambda_s = \frac{\lambda_{D_i}}{\sqrt{1 + \lambda_{D_i}^2/\lambda_{D_e}^2}} \tag{2.41}$$

Seeing that $T_e \gg T_i$, $\lambda_s \approx \lambda_{D_i}$. Essentially, the factor 2.40 means that ions outside of the Debye sphere can still apply a force to the particle without direct interaction. [30]

2.3.5 Thermoforetic force

The last significant force on airborne particles in the setup is the thermoforetic force. It is caused by temperature gradients in the setup. The idea is that hotter, more energetic particles transfer more momentum to the particles than colder, less energetic particles do upon colliding. The average force of these collisions is therefore directed along the thermal gradient, toward colder areas. The thermoforetic force is given by

$$\vec{F}_{th} = -\frac{32r^2}{15v_{th}}\left(1 + \frac{5\pi}{32}(1-\alpha)\right) k_T \vec{\nabla} T_g \tag{2.42}$$

with v_{th} the gas temperature, α an accommodation constant assumed to be unity for temperatures below 500 K, k_T the Boltzmann constant and $\vec{\nabla} T_g$ the temperature gradient of the gas. [31]

2.3.6 Adhesive forces

When an airborne dust particle eventually lands on a surface, a few more effects arise. The adhesive forces at micrometer scale in this setup consist of two main components, the Van der Waals force and the capillary force. [32]

Van der Waals force

The Van der Waals force is an attractive force between surfaces at close range for the purposes in this thesis. For increasingly small dust particles it becomes more and more important. It also heavily depends on surface topology. Hamaker [33] approximated that for two macroscopic bodies at close approach, the VDW force is equal to

$$F_{vdw} = \frac{A r_1 r_2}{6(r_1 + r_2)d^2} \tag{2.43}$$

where A is the so-called Hamaker coefficient, which is a material dependent value between $10^{-19} - 10^{-20}$ J, r_1 and r_2 are the radii of the two bodies and d is the distance between the surfaces, typically between 0.1-1 nm. For a particle-surface interaction this reduces to

$$F_{vdw} = \frac{A r_p}{6d^2}. \tag{2.44}$$

Capillary force
The second adhesive surface force is caused by a water layer on a surface. The water surface tension then exerts an attractive surface force on a particle when it lands. Water at room temperature vaporizes at approximately 2.3 kPa. Though the experiments were done at a lower pressure, it is possible not all water has vaporized, especially in the thin gas layer. Still, the force due to capillary action has been neglected.

2.3.7 Lofting force

The Plasma lofting force, recently studied by Heijmans [34], is able to repel particles from a surface near a plasma. Its origin is still unknown, though studies have accounted it to the electric field of the plasma sheath [35] or surface modification by a plasma. As for its measured effect, it is a small repelling force that will make it harder for particles to stick to a surface where a plasma sheath exists.

2.3.8 Flow

The flow in our system is an important factor for particle transport. The effects of the flow on the particle will be described in this subsection. From equation 2.26, the Reynolds number can be calculated and lie in the range of 10-100 depending on the location in the setup. This means that the flow can be seen as laminar as $Re \ll 2300$ and can be described by a Poiseuille flow. The radial part of the flow, which is the main part of the experiment, can easily be calculated and is of no concern. The particles enter the system before the developed flow is reached, so entrance effects have to be taken into account.

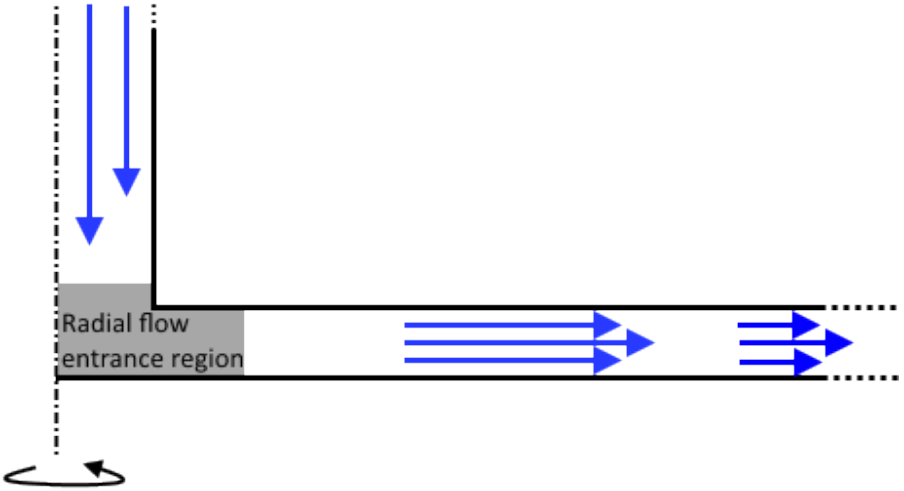

Figure 2.5: Schematic drawing of the flow in the setup.

Entrance effects
Before a flow is fully developed, there exist entrance effects to adjust for the change in optimal flow profile. In the first part of the duct, there will be a 'core' in the middle in which viscous effects are effectively zero. Outside of this core there exists a boundary layer. In this layer the profile is dictated by viscous forces due to a high shear stress. The length over which this entrance profile evolves into the fully developed flow is called the entrance length of the hydrodynamic entrance region. This is given, in the case of laminar flow, by

$$L_e = D(C_1 + C_2 Re) \tag{2.45}$$

with D the typical length scale, in this case the width of the duct and C_1 and C_2 dimensionless coefficients equal to 0.5 and 0.05 respectively. [36]

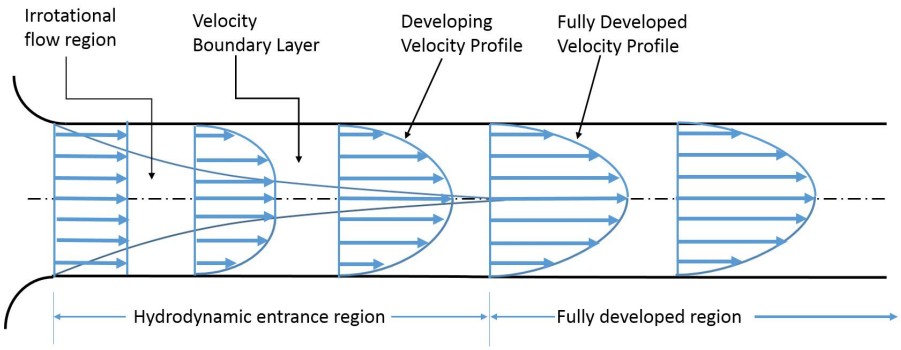

Figure 2.6: Schematic drawing of the evolution to a fully developed Poiseuille flow. [37]

Flow profile

The developed flow profile between the two plates can be approximated by a radial Poiseuille flow. The flow is axisymmetric around the vertical axis of the setup, so the two-dimensional Poiseuille flow is enough to determine the flow everywhere. It is given by

$$u(z,r) = u_{max}(r)\left(1 - \frac{4z^2}{d^2}\right) \tag{2.46}$$

where the plates are located at $z = \pm d/2$. The velocity is dependent on the radial position as the volume flux is constant through a surface with increasing radius. The volume flux is equal to

$$Q = \int_{-d/2}^{d/2} 2\pi r u(z,r) dz = \frac{4}{3}\pi r d u_{max}(r). \tag{2.47}$$

Now equations 2.46 and 2.47 can be combined into the following flow profile

$$u)z,r) = \frac{3Q}{4\pi r d}\left(1 - \frac{4z^2}{d^2}\right). \tag{2.48}$$

This equation holds for all $L_e < r < r_{plate}$

Vertical flow-induced forces

A particle that travels with this flow will experience vertical forces due to pressure gradients. The most important two being the shear gradient force and the wall-induced lift force. [38] The shear gradient force arises from the velocity gradient of the flow profile. The difference in relative flow velocity at the top and bottom of the particle will push the particle away from the center towards the walls [39]. The wall-induced lift force however pushes particles away from the walls of the flow duct. [40] This is caused by the deformation of streamlines due to the particle. Near a wall, the flow will bend around the particle in a way that creates a lower pressure at the side of the particle that is furthest away from the wall. As a result of this effect the particle is pushed from the walls. [41]

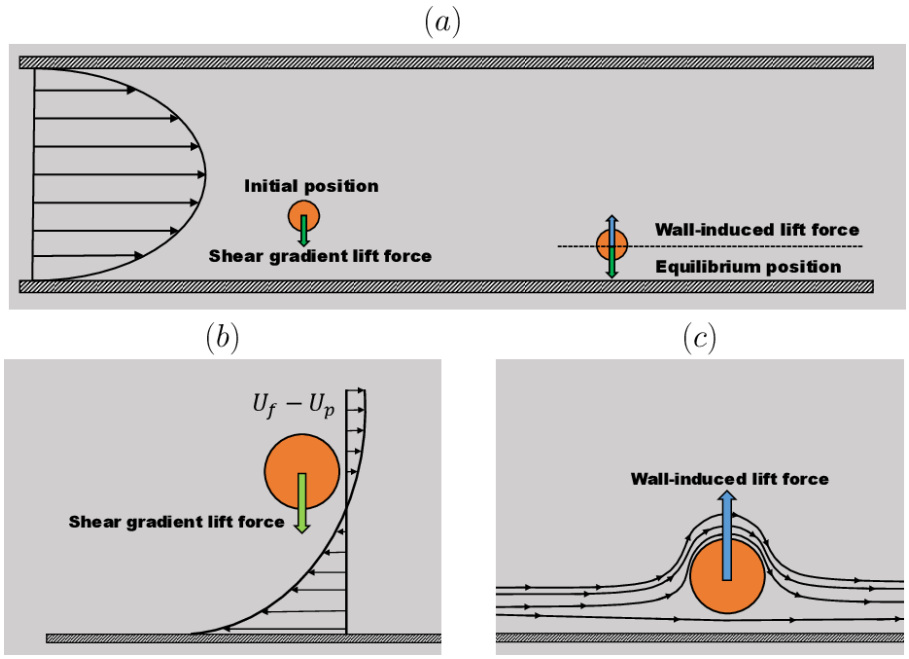

Figure 2.7: Schematic of the workings of vertical flow-induced forces. [42]

Chapter 3

Experimental Setup

In this chapter, the experimental setup used for the measurements is explained. Firstly, the general idea of the vacuum seal design will be discussed in section 3.1. Then, the restrictions and choices used for translating this to a test setup for investigating the main processes and properties are laid out in section 3.2. The setup and its parts are introduced and described in section 3.3. Lastly, the method of obtaining results are explained and discussed in section 3.4

3.1 Design Restrictions

As mentioned in the introduction, the vacuum seal is purposed for a SCARA-robot in high vacuum1.1b. This constraints the design choices to be able to fit in the small space of the joints of the SCARA-robot. The most obvious restriction is that the seal must be cylindrical, as the robot arm should be able to rotate without any axial asymmetries. The top and bottom arms are separated by a small gas layer of at most 20 mm, which acts as an air bearing to ensure frictionless rotation. The seal has to act in this gas layer, where the contamination will take place. As the gas layer cannot be too large, the vacuum seal design is also limited in its height. Also, the seal may not have solid components in the gas layer, as this will affect the air bearing. One last geometrical design constraint is that the contaminants enter the seal from the center in a circular area of 15 mm, and move outward. Outside of the robot joint gas layer, there should be no contaminants, as this is the purpose of the seal.

The robots currently operate in a chamber that is filled with nitrogen at 2 Pa without flow. The flow within the gas layer of the robot arms is redirected so that it has little effect on the flow in the vacuum chamber. This requires high-end equipment which was not available during this project. Using the available equipment and to ensure proper flow within the gas layer, the experiments were done at 1200 Pa. Either argon or air were used as background gas.

The last main restrictions dictate that the maximum temperature gradient between the robot arms is 20 mK. This restriction is not considered part of this project, as the focus lies in researching the workings of the seal rather than delivering a finished product.

3.2 Design Choices

A large number of choices can be made for a first setup, and it can be tedious to test every single one. Therefore it is useful to limit ourselves to the best expected designs. The following subsections describe the thinking process which led to the final design of the experimental setup.

3.2.1 Surface

The primary restriction with regards to the surfaces of the vacuum seal is that the top and bottom surface should have a gas layer between them. The shape of the surfaces is not restricted. The preeminent options are a flat surface, an incline, and a 'labyrinth'. A flat surface was chosen for this research because it is easy to measure contamination from the plates. However, for an end product it may be useful to look into the other two options. An incline has the advantage of gravity working more strongly to slow down the contaminants, but the effect may be too small depending on particle size and flow velocity. A labyrinth has an interesting flow profile and more surface area that lowers radial velocity of the particles. This can allow other forces to act longer as well as catch particles on the walls perpendicular to the radial flow.

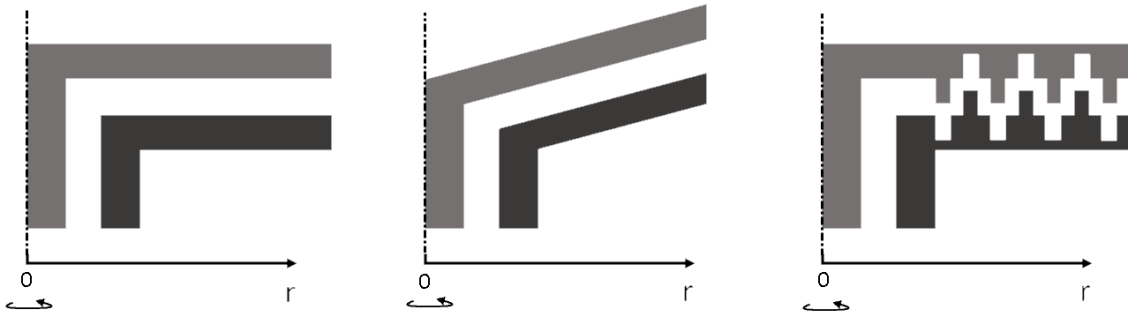

Figure 3.1: Schematic drawing of gas layer with different surface geometry options. a) flat, b) incline, c) labyrinth.

3.2.2 Driving force

Considering the fact that the objective is to move particles in a gas flow, a number of forces can be used. The main candidates are electric forces, inertial forces, optical forces and thermoforetic forces. Moving parts in the setup can interfere with the gas layer and the workings of the robot arm, ruling out inertial forces as driving force. Inertial forces as a result of particle movement however, should still be kept in mind for calculations. Optical forces are possible since they do not interfere with the gas, but are too weak to stop larger contaminants before they leave the gas layer. Thermoforetic force is not possible, as the thermal gradient design restriction prevents this from being a driving force. This leaves us with electric forces, as it is easy to induce. This however does mean that the contaminants need to be charged, leading to a more complicated design.

3.2.3 Particle Charging

The use of an electric field as the driving mechanism in the setup requires the charging of the contaminating particles. This can also be done in a number of ways. The options are triboelectric charging, electron beam charging, UV-charging, and using a plasma. Triboelectric charging is hard to control using many particles, and can therefore not be used as primary charging mechanism. Involuntary triboelectric charging does occur between contaminants and should be kept in mind during the experiments. Because of the geometry of the setup, using an electron beam and UV-light is not feasible. This leaves the use of a plasma. Since temperature gradients are not wanted, this further limits how a plasma should be generated as a thermal plasma is not wanted. Corona discharges are hard to generate without altering the gap between the robot arms. An inductively coupled plasma is hard to generate considering the cylindrical geometry of the setup. The best option by far is using a capacitively coupled plasma. In particular, a dielectric barrier discharge (DBD) was chosen. The reason is that it keeps the gap width constant while leaving the option to choose where the plasma is generated without generating sparks.

3.3 Main Setup

Figure 3.2 below shows an overview of the main setup and a photograph of the actual setup.

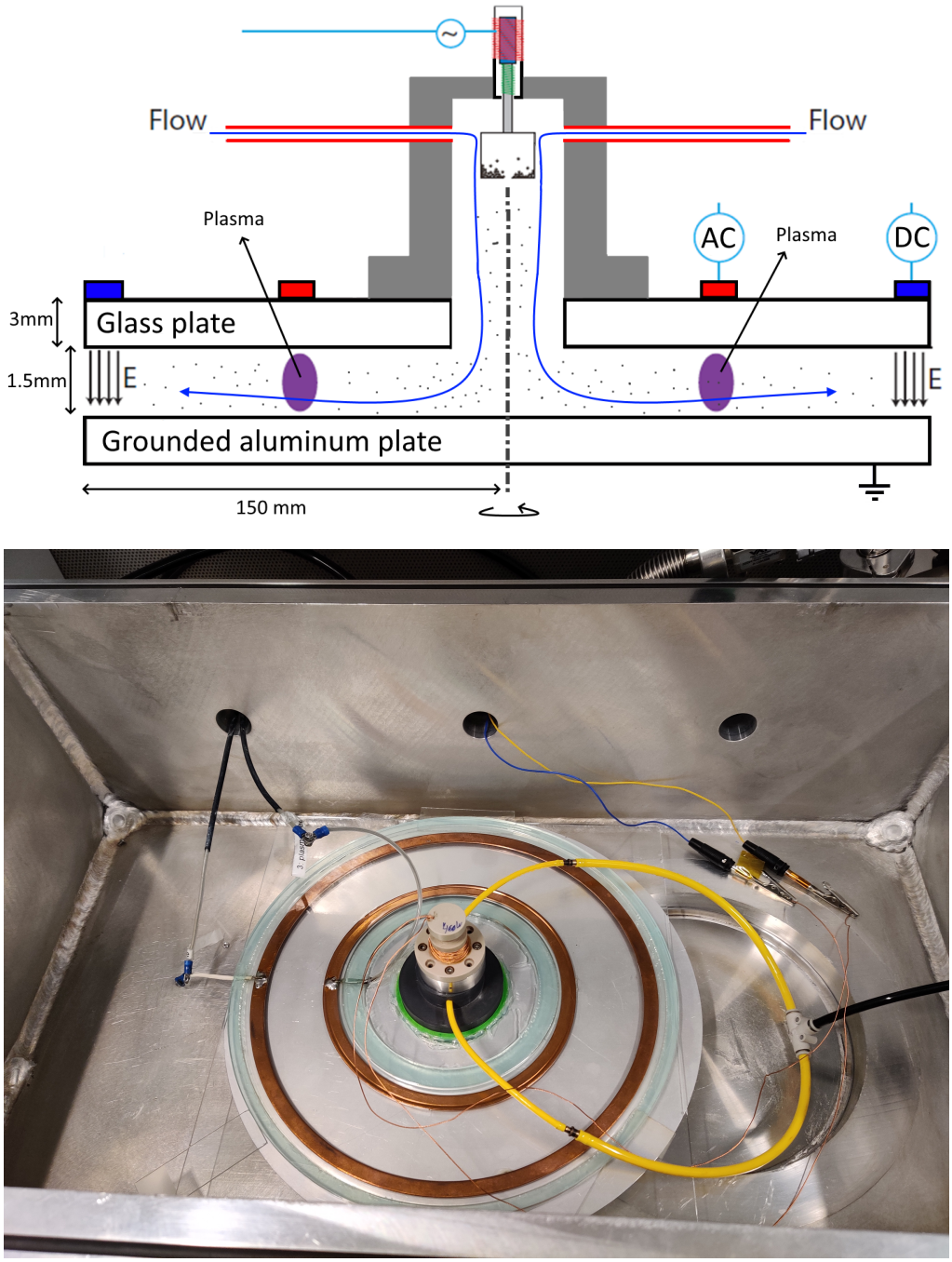

Figure 3.2: a) Schematic drawing and b) photograph of the main setup.

3.3.1 Setup Workings

The experiments take place in an aluminum vacuum chamber with inner dimensions of 650x350x200 mm and a pressure of 1200 Pa. The pressure is a result of the balance between the

vacuum pump (Edwards XDS-10) and a controllable inflow. The inflow was kept constant at $5 * 10^{-5}\ m^3/s$ for all experiments. The inflow is directed towards the middle of the setup resembling a SCARA-robot joint. This setup consists of a 1 mm thick round grounded aluminum bottom plate with a diameter of 320 mm and a 3 mm thick 300x300 mm square glass upper plate separated by a 1.5 mm wide gap. This gap thickness was chosen as it approached both the maximum radius for a low power plasma and the real-life application value. Glued to the top of the glass plate are two copper rings acting as electrodes to generate an electric field or plasma. These rings are insulated by a layer of epoxy glue. In the center of the glass plate there is a circular hole with a diameter of 25 mm through which particles are injected using a particle dispenser. This dispenser as well as the tubes for the inflow are held by a 3d-printed object. The entire setup is placed inside of a cross-flow cabinet to remove background particles in the measuring environment. This leads to an effective cleanroom classification of at least ISO 3.

3.3.2 Electrodes

To generate a plasma and an electric field, two electrodes are glued on top of the upper plate. These electrodes are circular copper vacuum gaskets. The inner electrode has inner and outer radii of respectively 76 mm and 86 mm. The outer electrode has inner and outer radii of 127 mm and 137 mm. The electrodes can be powered with a sinusoidal voltage of 875 V at 22.4 kHz to generate a plasma. The alternative is a 400 V DC voltage to generate a DC electric field.

3.3.3 Particles

To simulate contaminants, glass spheres were used. The glass spheres have a non-homogeneous size distribution of 44 μm or smaller. The particles enter the system by use of a particle dispenser. The dispenser is activated by powering a coil surrounding an iron rod. The rod is connected to an aluminum cylindrical container with a height and diameter of 10 mm. The container has a 50 μm hole in it. Upon switching power to the coil, it acts as an electromagnet, moving the rod and container up and down by approximately 15 mm, releasing a small cloud of particles. Controlling the dispenser is done via an external program. Pulses of 100 ms are sent each second of 2 A at 24 V. Because of the particle distribution, no single use of the dispenser releases the same particles.

Another effect of the dispenser is that the particles will be triboelectrically charged. Particles rubbing against each other will lead to charge accumulation. In general, larger particles will acquire a more positive charge while smaller particles will often charge more negatively [43]. These charges are not feasibly measurable as they can change during the measurements. While triboelectric charging should still cause a total charge of zero, triboelectric charging also can happen between particles and the aluminum container, yielding a net positive total charge on the particles. According to theory the absolute maximum charge per particle will be around $(1-5)*10^3$ e [44]. This has a few consequences. The most obvious is that particles will experience electric forces in the setup before they have been charged by a plasma. Another consequence is that the balance of ions and electrons in the plasma is altered. However, this effect is considered negligible as the plasma density far outweighs the amount of particles released. Lastly, the charged particles can attract each other, leading to clusters. As the larger particles often have the highest charge, they can attract multiple smaller particles. This has been observed in a SEM as seen below in figure 3.3

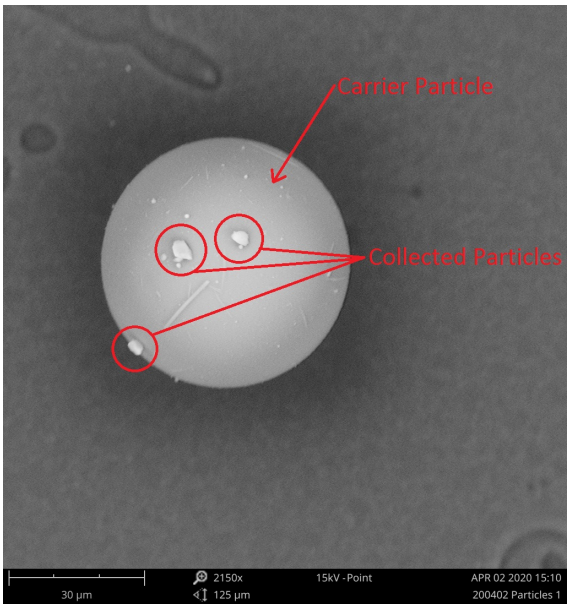

Figure 3.3: SEM image of a glass particle cluster.

Here, a cluster formed on a relatively large ($r > 5\mu$) particle can be seen. This 'carrier' particle has collected a lot of smaller ($r < 5\mu$) particles, the largest of which have been encircled in red. The cluster is sucked up into the particle counter as a whole, but the particles are measured individually.

3.4 Measurements

Measurements of particle locations are done after the experiment. This is due to the complicated nature of the experiment, as the area of interest is very narrow, surrounded by a large aluminum box while working with high voltage.

After the experiment, the upper glass and bottom aluminum plate are removed from the vacuum chamber and put onto a Phoenix CMS-P1 contact plotter. The pen of this plotter has been replaced with a suction cup attachment which is connected to a Solair 1100-LD particle counter, which sucks up particles and filters the contaminated air afterward. The contact plotter can be programmed to move across the surface of the plates. This is done by using a MatLab script which sends MS-DOS commands at precise time-intervals. The particle counter is synchronised with this movement, scanning it by sucking up the particles. Background particles are of small influence due to the entire setup plus measurement method being placed in a cross-flow cabinet.

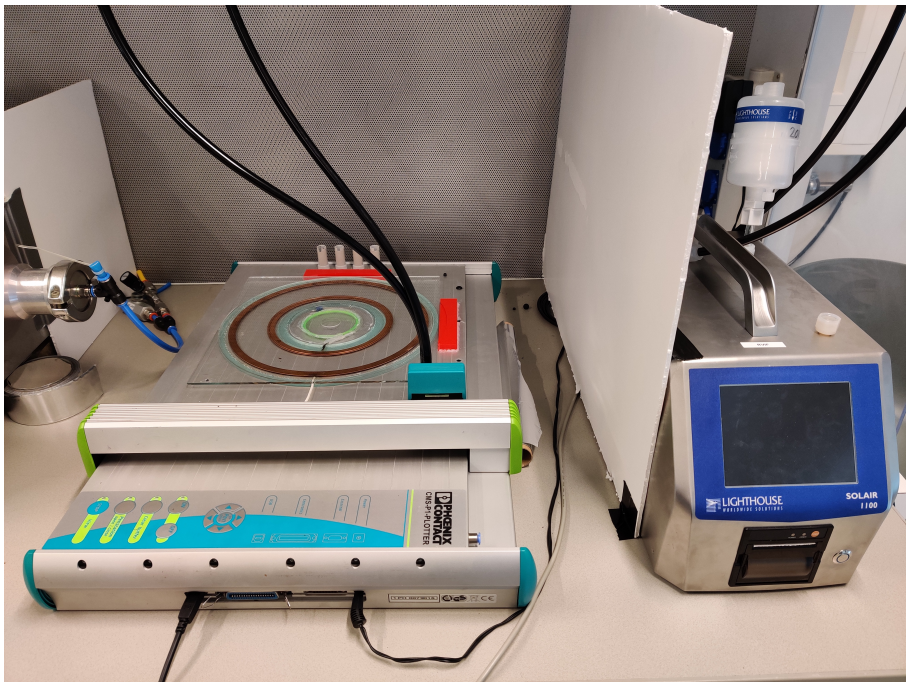

Figure 3.4: Photo of the particle counter and contact plotter measurement setup.

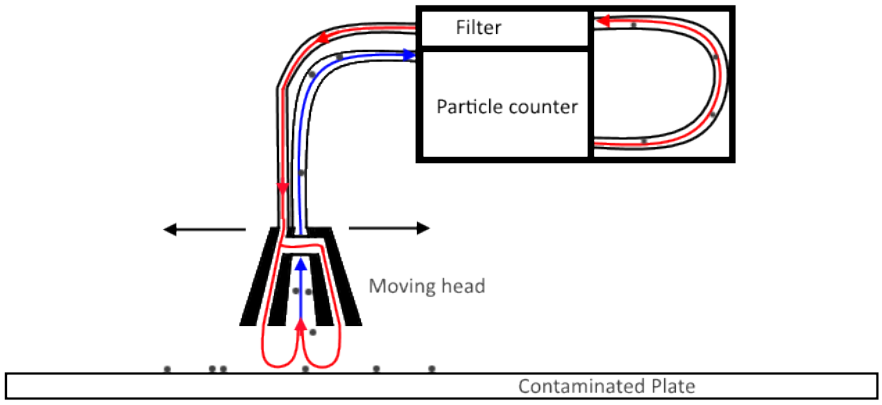

Figure 3.5: Schematic drawing of the particle counter and contact plotter measurement setup.

The obtained data is a list of particle amounts measured per size in time intervals of 10 seconds. 10 Seconds of measure time per location ensures that no particles are still left in process of being measured. Another MatLab script then assigns each value of measured particles to the correct x and y coordinate of the measurement. A heatmap can then be made of the plate, visualising how many particles per size are measured where on the plate. An example measurement is shown in figure 3.6 below.

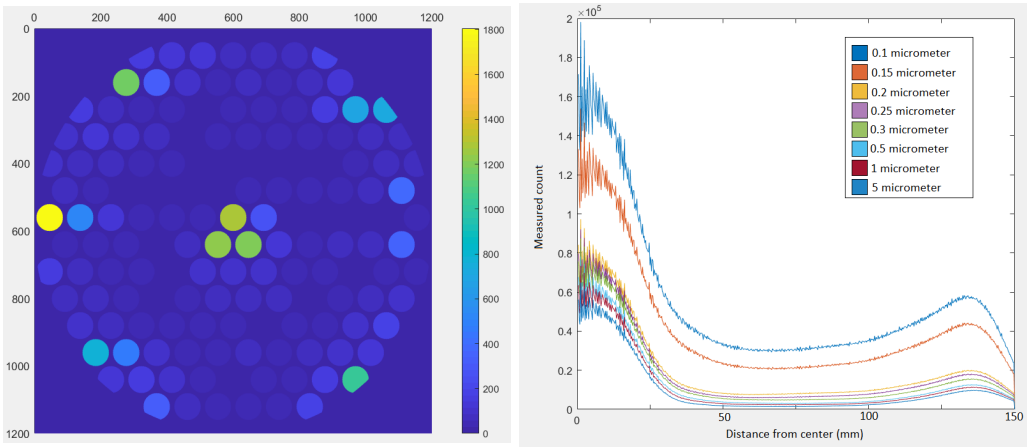

Figure 3.6: a) Heatmap of a particle distribution on a plate. Shown is the amount of measured particles versus location on the plate in arbitrary units. The yellow colored areas have more particles while the blue colored areas have less or no particles. b) Graph that shows the amount of particles divided by 2 pi times the radius of where it was measured, versus the distance from the center in arbitrary units.

The data can also be put in a graph that shows the amount of particles versus distance from the center. This is useful as it allows for simulation verification and the calculation of particle paths. The particle amounts in the graph are divided by 2 pi times the distance from the center where it was measured. This ensures that the measurement area is distance-invariant.

The setup is cleaned three times after each measurement using isopropyl alcohol. Measurements have shown that the amount of particles measured directly after the cleaning process is drastically lower. For the smallest detected particles of 0.1 μm, at least 70% fewer background particles are measured. For 5 μm particles, at least 95% fewer background particles are measured after cleaning.

Chapter 4

Simulations

This chapter will combine the theory and the geometry and process parameters of the experimental setup into a working COMSOL Multiphysics simulation. A simplified version of the setup will be used to examine particle paths. The final positions of these particles can then be compared to those of the physical experiments to validate the model. The model can then be used to simulate virtual experiments to optimize the effectiveness of the vacuum seal.

4.1 Time-independent model

A time-independent model is made by first using geometries that represent the experimental setup. A 2-D axisymmetrical geometry was chosen because computationally it is the least intensive while still representing the setup correctly. Only the main part of the setup was modeled. The vacuum chamber and gas inlet are not modeled directly. Instead boundary conditions were used to best simulate the effects on the main setup. The resulting base model is shown in figure 4.1 below.

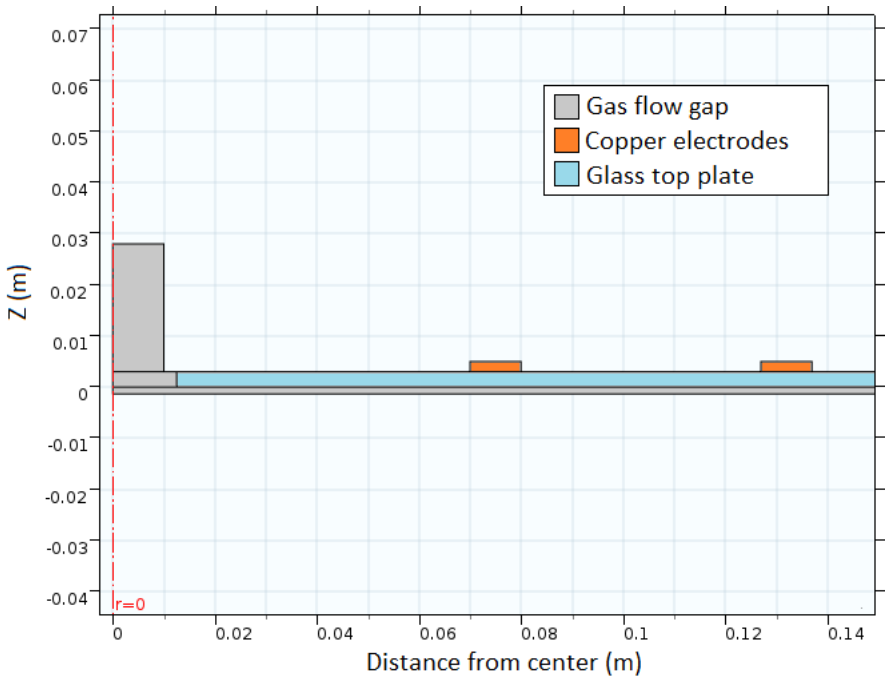

Figure 4.1: 2-D Slice of the base geometry of the model. Colors have been added in this picture to represent different materials. Gray for argon, blue for silica glass and orange for copper.

4.1.1 Flow

The first part of the model and one of the main driving mechanisms for particle movement is the flow in the system. As mentioned in chapter 3, the inflow has been measured to be equal to $5 * 10^{-5}$ m^3/s, while the outflow is governed by a static pressure equal to 1200 Pa. Together with calculated Reynolds and Knudsen numbers of respectively $Re \approx 36$ and $Kn \approx 1$, a laminar (non-creeping) flow is used with non-slip wall conditions. The resulting velocity distribution is show in figure 4.2.

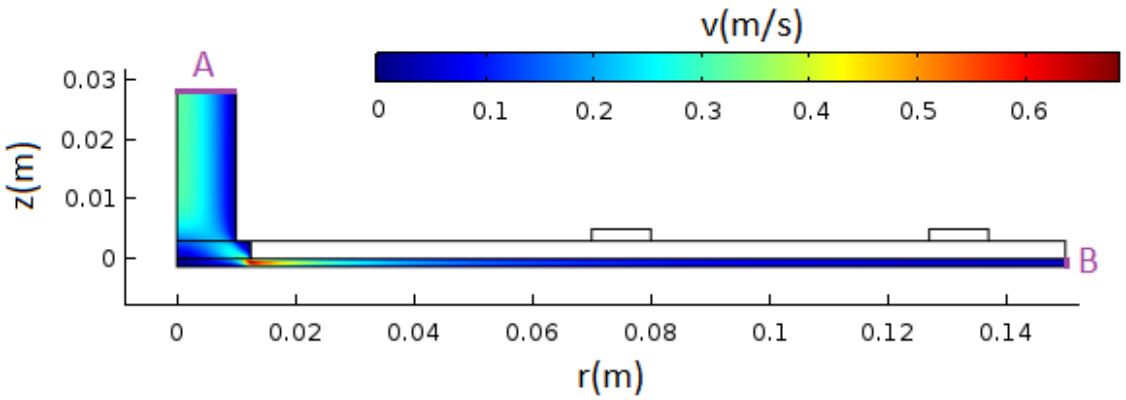

Figure 4.2: 2-D Slice of the flow velocity distribution in the model. A and B mark the location of the inflow and outflow boundary conditions respectively.

A few things are of note here. Firstly, while the flow in the gap quickly evolves into a radial Poiseuille flow, the entrance effects in the center are too important to ignore. a relatively high velocity and velocity gradient appears at the start of the gap. Furthermore, the exact center of the setup has a very low r-component to the velocity. This can cause a lot of particles to have gravity as a main driving force, without being allowed to enter the gap. Lastly it should be noted that the radial velocity quickly drops to near zero in the gap. This means that any manner of slowing down particles can prove very effective for avoiding contamination to leave the setup.

4.1.2 Electrostatics

At some point, a DC voltage will be applied to an electrode to create an electric field. This voltage is too low to generate a plasma. This part of the model is therefore very uncomplicated. The bottom plate is grounded while the electrode has a constant potential of 400 V. The resulting electric field components are shown in figure 4.3.

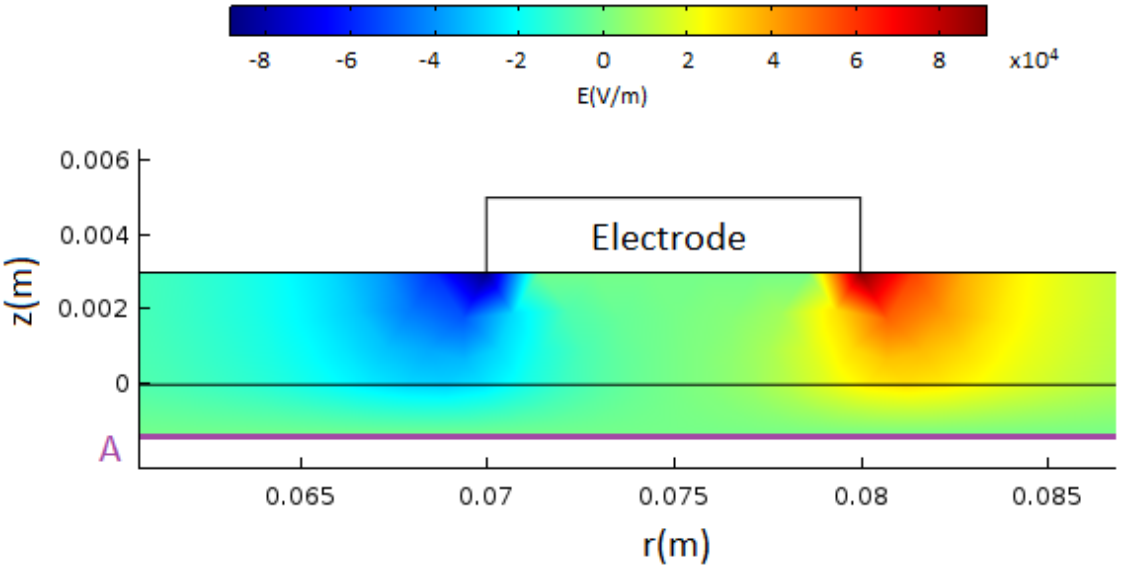

(a)

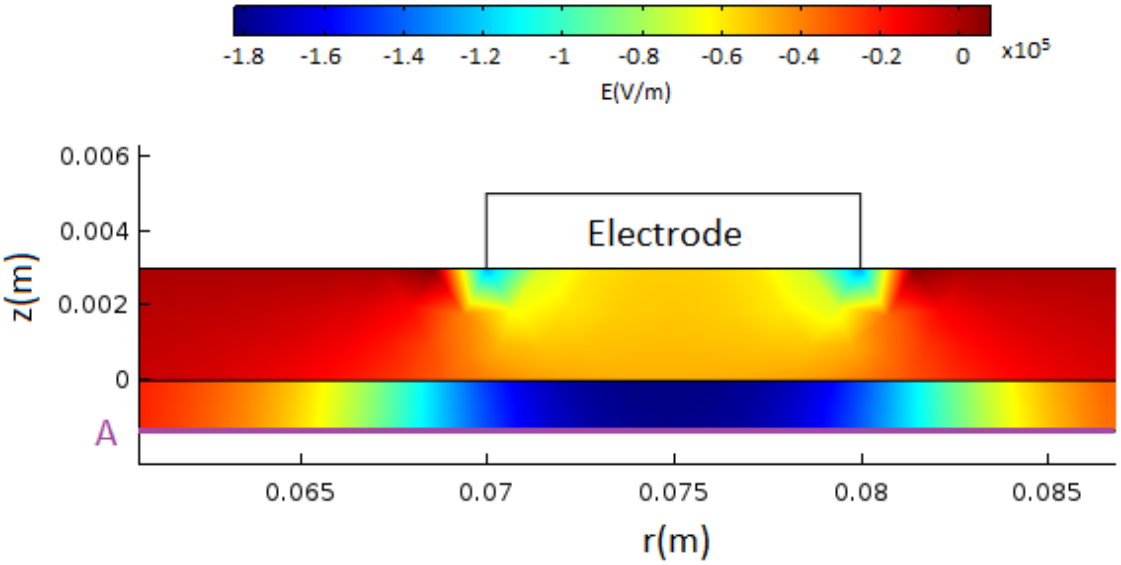

(b)

Figure 4.3: a) r-component and b) z-component of the electric field directly underneath a 400 V DC powered electrode. Boundary A is grounded.

When the voltage polarity is switched, the direction of the electric field switches as well. The z-component is much stronger than the r-component and consistent over the gap height. The r-component should not be neglected however, as it can cause particles to be slowed down or sped up depending on their charge, especially at the top half of the gap. This may prove insightful for the spread of particle distributions near the electrode on the top plate.

4.1.3 Plasma

While the plasma is certainly time-dependent, as it relies on an AC-plasma and dynamic processes, it can be considered as time-independent in the setup. The reason for this is that the timescale for which the plasma affects the particles is much larger than the timescale for changes in the plasma

itself. The particles therefore only experience time-average plasma.

Modelling a 2-D plasma including afterglow is a difficult and time-consuming process. It is not feasible to combine the plasma model, the flow and the particle-tracing simulation for computational reasons. A solution that allows for fast and satisfactory plasma results is to use a 1-D plasma model. This model is disjoint from the rest of the simulations and merely provides boundary conditions for electrostatic properties in the setup. This model is then theoretically expanded upon using theory for afterglow and particle charging. This drastically decreases the computation time for the simulations which allows for faster optimization of the model and the theoretical optimal setup.

Figure 4.4 and 4.5 show the results of the simplified 1-D plasma model. The left part of the 1-dimensional simulation is the glass dielectric barrier, which is connected to a terminal. The right part is the gas layer, which is filled by argon and grounded at the rightmost edge. A sinusoidal voltage is applied to the terminal with an amplitude of 875 V and a frequency of 22 kHz. Shown are the electron energy and average potential in the gas gap.

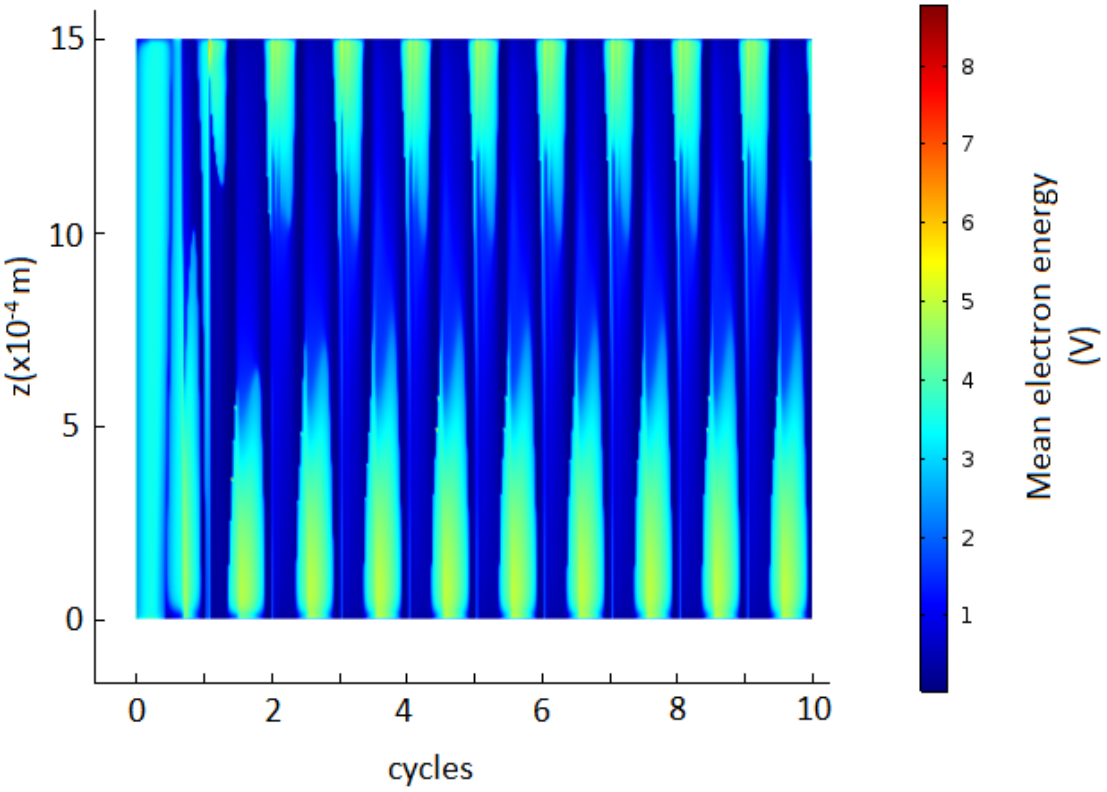

Figure 4.4: Mean electron energy distribution over the gap over the first 10 AC cycles. The x-axis shows the distance from the upper plate while the y-axis shows the first 10 cycles of the AC-voltage.

The model predicts a time-averaged potential distribution as shown in figure 4.5 and a time and space averaged electron temperature of 2 eV. Both of these will be used as boundary conditions in determining the charging effect and electrostatic force on the particle.

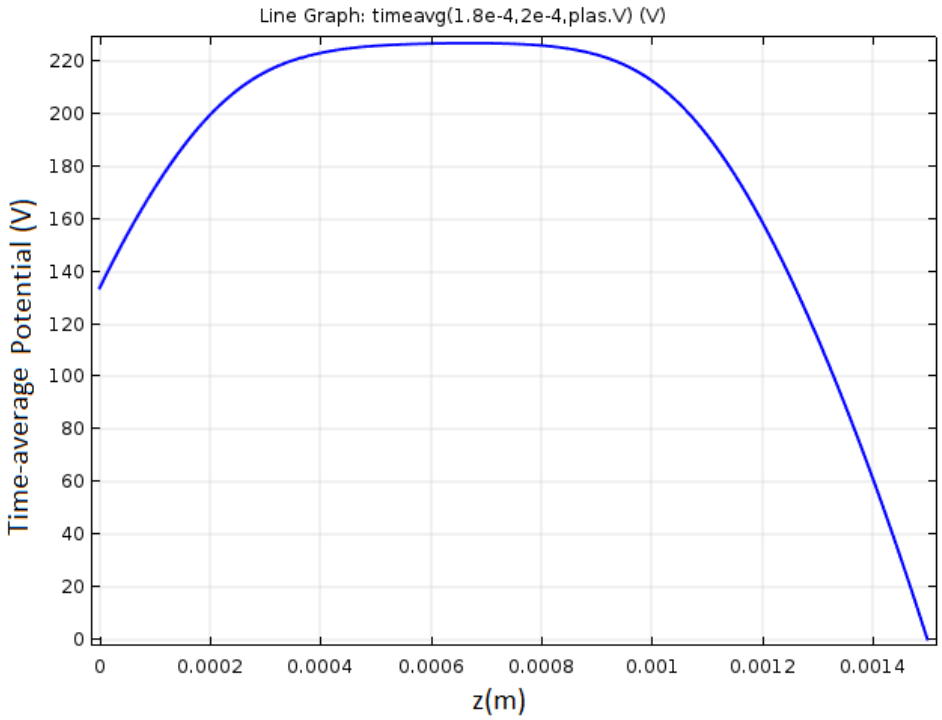

Figure 4.5: Average potential distribution over many cycles after an equilibrium has been reached.

4.2 Particle-tracing

Now that the time-independent part of the model is done, the COMSOL particle-tracing module can be used to simulate particle trajectories. As the particle dispenser in the setup works randomly, a uniform distribution of initial particle locations has been chosen for the particle inlet. This assumption was made for simplicity's sake and can be altered if necessary. When a particle leaves the main setup, at $r = 150$ mm, the particle disappears from the simulation. Particles that touch any wall of the setup stop in place, assuming that adhesive forces strongly outweigh any forces that might pull the particle from the surface. Particles are also not assumed to bounce because of their low vertical velocity [45]. The simulations were done assuming a particle diameter of 2.5 μm and a density of 2200 kg/m^3. Figure 4.6 and 4.7 show the results of the simulation in the case without active electrodes.

From these figures, a mostly uniform distribution arises. As expected, Due to the low radial velocity in the center of the model, a peak in particle density arises. As the radial velocity decreases with increasing radius, there is a small increase in particle density near the outer edge of the setup. This increase in density represents slow particles that are unable to leave the setup before settling.

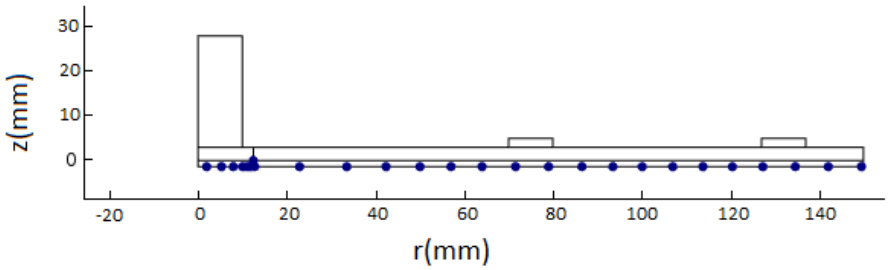

Figure 4.6: 2-D Slice of a particle-tracing simulation using only flow. Every blue dot represents the position of one out of N=100 particles after 5 seconds All particles have landed on the bottom plate

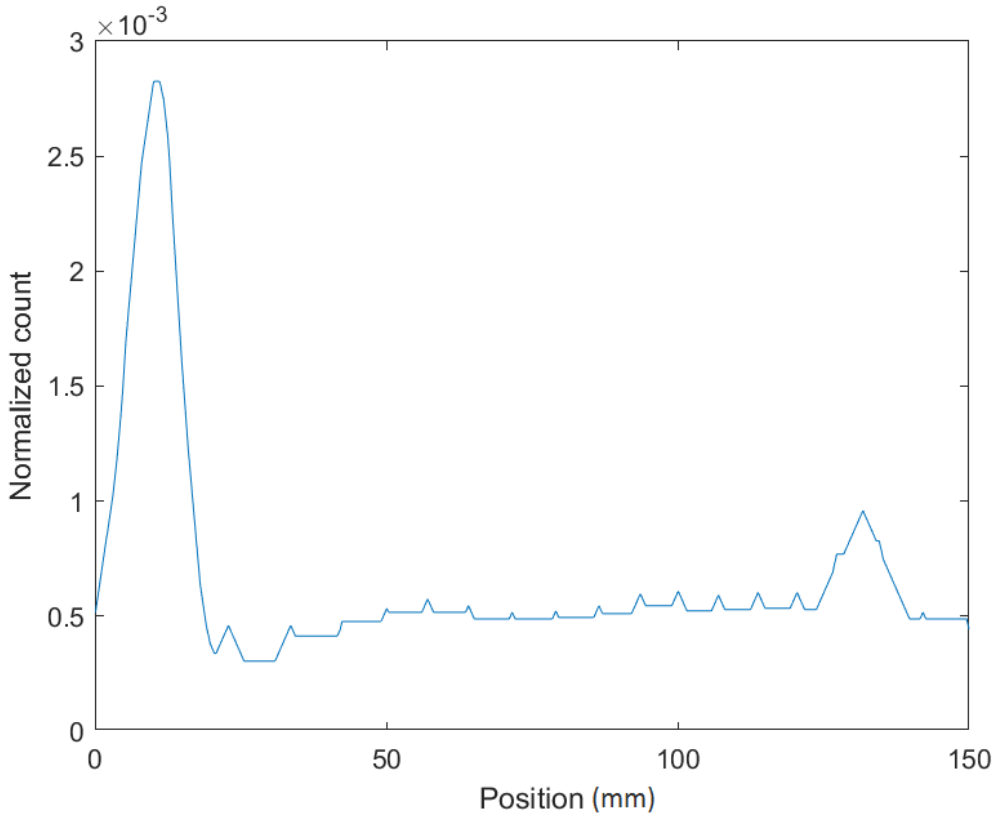

Figure 4.7: Normalized particle density of the flow-only simulation.

In the case of a DC powered electrode, the previously unused inner electrode will be powered with a constant 400 V. Both the terminal as well as the particles can have a positive or negative polarity. Using charge distributions measured from the same injection system by Heijmans [46] as a starting point, the simulation can later be compared to the results in order to estimate the charge distributions in this setup. Since the negative and positive particle distributions are not equal [47], the charge distribution is centered around a mean charge of 10 e with a standard deviation of 20 e. For larger particles, the absolute charge will be higher and more often positive, coinciding with previous studies [43], [48] The simulation results and accompanying particle distribution graphs are shown in figure 4.8 below.

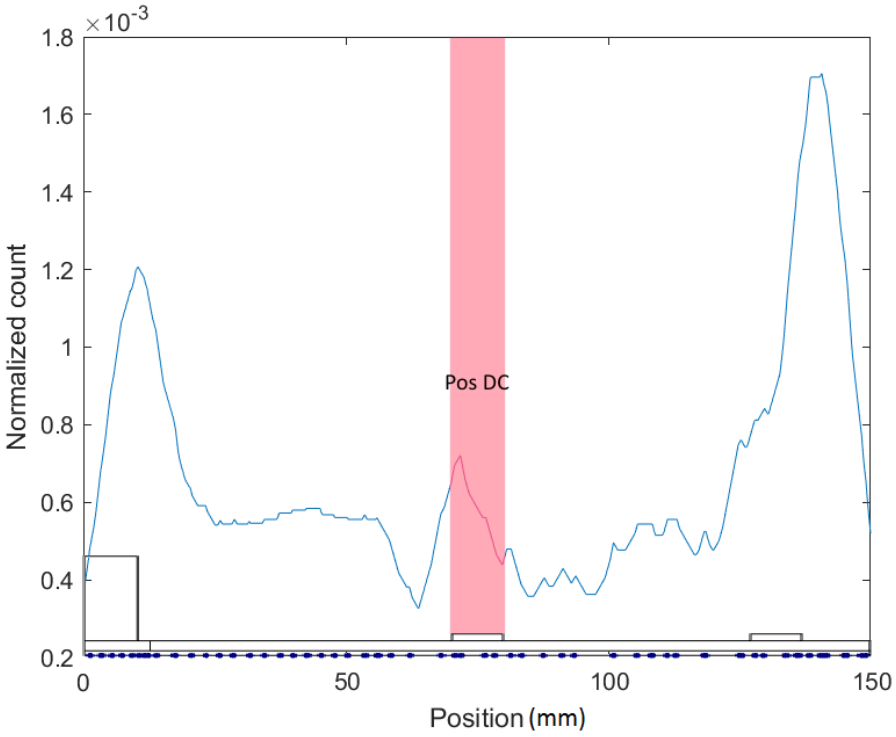

(a)

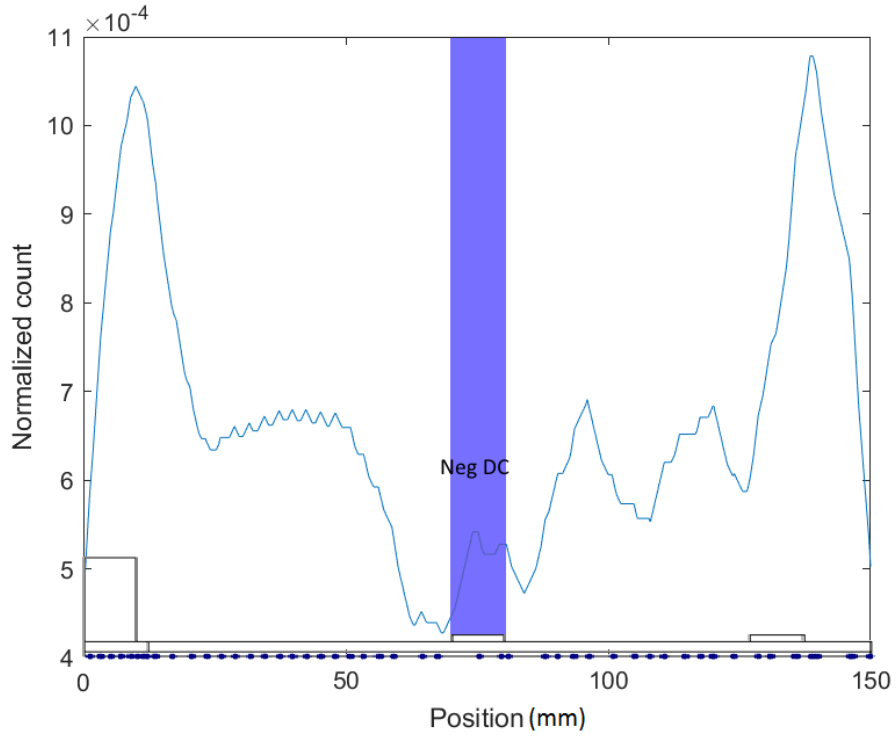

(b)

Figure 4.8: DC simulation result of the normalized particle density on the bottom plate. for an applied voltage of a) 400 V b) -400 V. The accompanying 2-D slice of the particle-tracing simulation has been added to the x-axis to show the location of the individual particles as well as the location of the powered electrode.

As expected there is a large increase in particle density near and after the electrode because of the resulting electric field. Smaller particles, which are more often negatively charged, are spread more evenly across the surface because the electric forces play a smaller role. The difference between the polarities is small, as the average charge of the particles is close to zero. This is because the plasma bulk of the triboelectric charge is caused by charge exchange between the particles themselves. The small net positive charge comes from triboelectric charging between the glass particles and the aluminum container.

Now that the initial charge of the particles is known, the plasma effects can be added to the model. The time-average plasma potential was put as a boundary condition in the gap. The calculated initial charge of the particles from the DC experiments was used. Finally, the OML and decharging theory was used to estimate the charge evolution of the particle due to the plasma. Since the charging time is very short ($\approx 10\ \mu s$), it is assumed that the particle charge in the plasma bulk instantly reaches the equilibrium charge of -700 e for a 2.5 μm particle. When the particle leaves the plasma bulk, the lower electron temperature and density cause the particle to decharge significantly. For a 2.5 μm particle, a final charge of -20 ± 10 e was used as this came closest to the experimental results. The results are shown in figure 4.9 below.

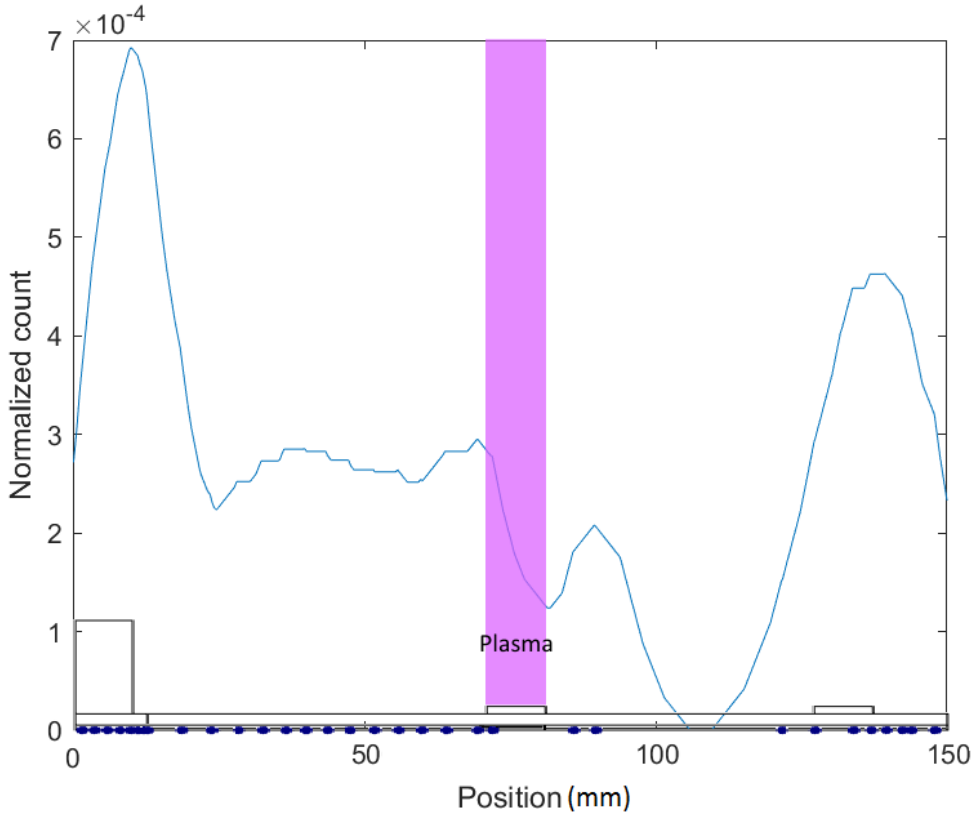

Figure 4.9: a) 2-D Slice of a particle-tracing simulation using a plasma at the inner electrode. b) Distribution of particles as a result of the simulation. The accompanying 2-D slice of the particle-tracing simulation has been added to the x-axis to show the location of the individual particles as well as the location of the powered electrode.

This shows a few interesting results. Primarily that of the two density increases in front of and behind the electrode. This is expected to be a result of positively charged particles that are repelled by the plasma potential. Another larger density increase can be seen at the edge of the simulation. Since there is no difference in the simulations at that location, this must also be an artifact of the plasma. This effect will later be discussed in the experimental results.

Now the final case of both a plasma and DC voltage is simulated. This is done for both a positive and negative voltage of 400 V on the outer electrode. The resulting electric field will affect the particles after they were charged by the plasma. The results are shown in figure 4.10 below.

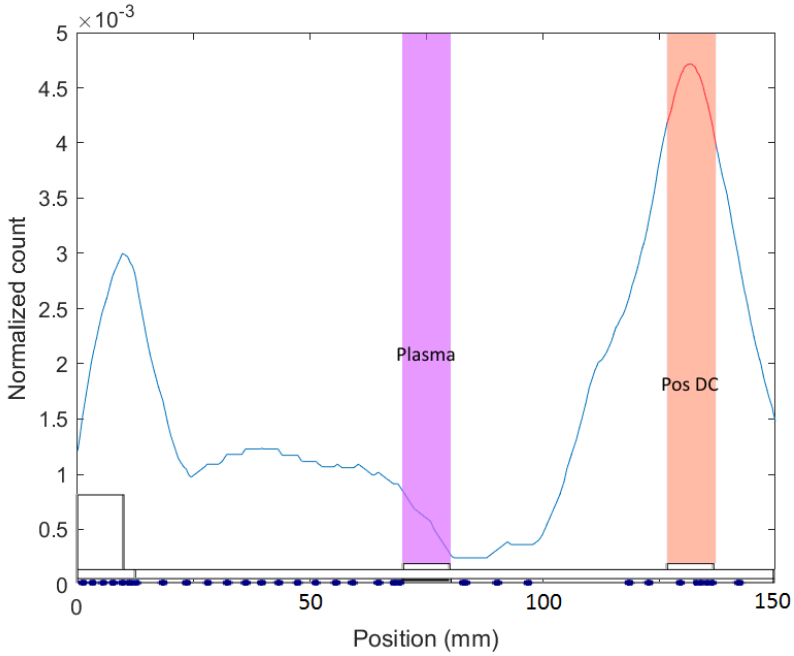

(a)

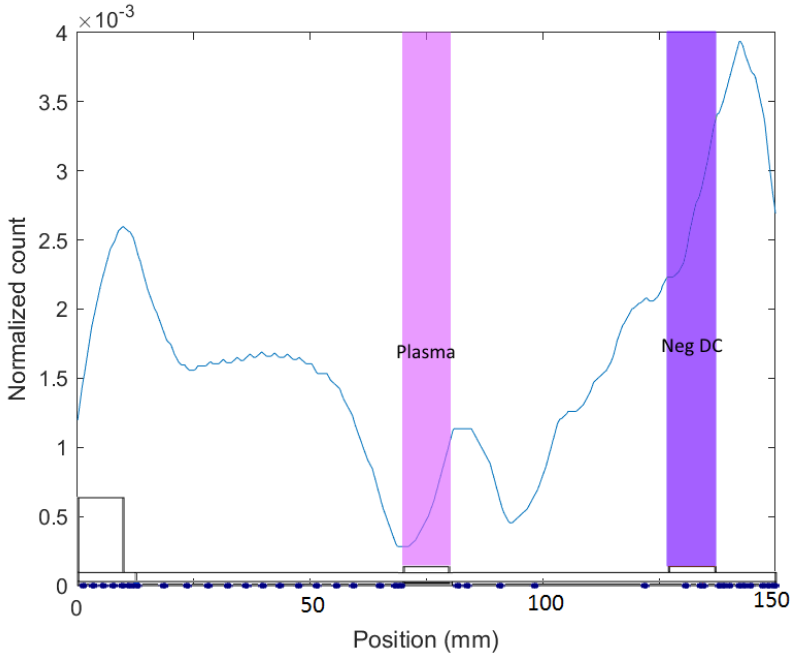

(b)

Figure 4.10: 2-D Slice of a particle-tracing simulation using a plasma at the inner electrode and a 400 V DC voltage at the outer electrode with a a) positive and b) negative polarity. The accompanying 2-D slice of the particle-tracing simulation has been added to the x-axis to show the location of the individual particles as well as the location of the powered electrodes.

As expected, the effects before the outer electrode are unchanged. The difference purely lies in the effect of the DC voltage applied to the outer electrode. In both cases it aids the settling of the particles. It is expected that these are the more highly charged particles, while the particles with a smaller charge are unaffected. On average, the particles will be charged negatively, therefore a negative DC bias will perform better. The leftover charge on the particles is rarely large enough for them to be lifted and adhered to the top plate, though not impossible. It does appear that this configuration is most effective for containing particles. The setup looks at least promising in achieving the premeditated goal.

Note that the simulation results only display the particle densities assuming every particle has a radius of 2.5 μm. Smaller particles are easier to control using electric fields. Smaller particles also tend to have a lower average negative charge, causing fluctuations to become more important. This might require a different approach to the seal, as the DC electrode might be detrimental in removing some of the particles.

Chapter 5

Results & Discussion

This chapter contains the description of the experiments and their results. These results are then explained and compared to simulations which have been discussed in the previous section. Each section discusses a subset of the experiments using parts of the total setup before combining everything into the final setup. Section 5.1 considers the setup without using electrodes. This will only take into account the flow of the system and the behaviour of the particles without an external field or plasma. Section 5.2 adds a DC electric field to the setup to establish the triboelectric charging. Section 5.3 finally adds the idea for the plasma seal both with and without a DC-field.

5.1 Control- and flow test results

The first few tests were done to determine the accuracy of the experimental process and the measurements. Also the 'neutral' situation is examined, where no electrical components are used. Figure 5.1 shows the normalized particle concentration on the bottom plate after cleaning it with isopropyl alcohol.

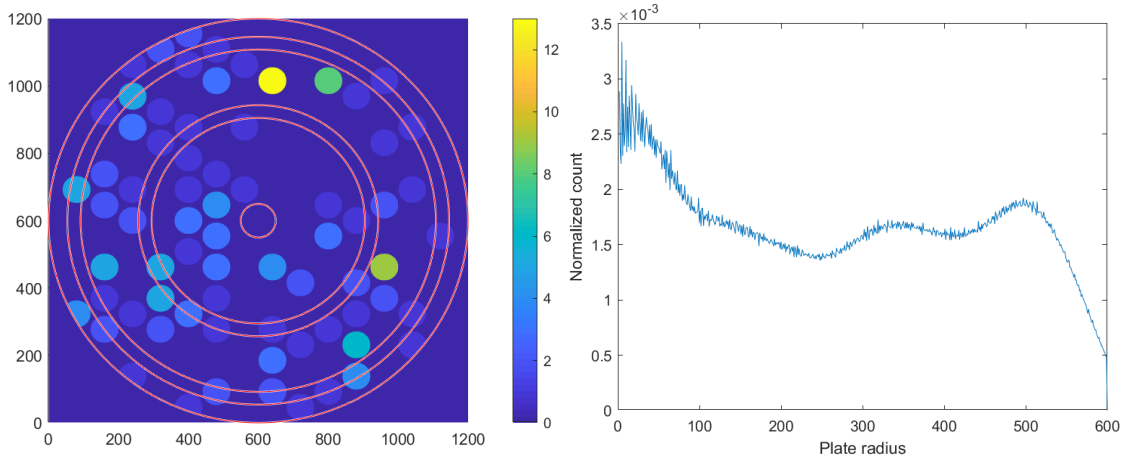

Figure 5.1: a) Heatmap and b) radial graph of particle concentration on a clean bottom plate. The x-axis in the graph represents distance from center to a maximum of 150 mm. The units in the graph are based on data points.

5.1.1 Measurement validity

The nature of the measurement process has the main disadvantage of not being able to measure during the experiment. This may allow effects outside of the experiment to play a role in changing the result of the experiment before measurement. This subsection explores the possible issues that may appear, how likely they may be and how they are corrected for if possible.

The final position of the particles on the plates is eventually measured outside the setup. A number of issues thus possibly exist between stopping the experiment and the starting the particle counting measurement. Particles can move due to repressurizing the vacuum chamber in order to take the plates out for measurement. Another possibility is that while moving the plates, particles may let go or be caught during the movement. To combat these possibilities, the chamber is pressurized back to atmospheric pressure slowly, over at least 2 minutes. The moving of the plates is also done slowly. This last concern unfortunately is not measurable.

The effect of changing the pressure in the chamber is measurable and appears significant compared to 5.1. The setup is prepared as normal and a vacuum was applied and removed. The effects are shown in figure 5.2.

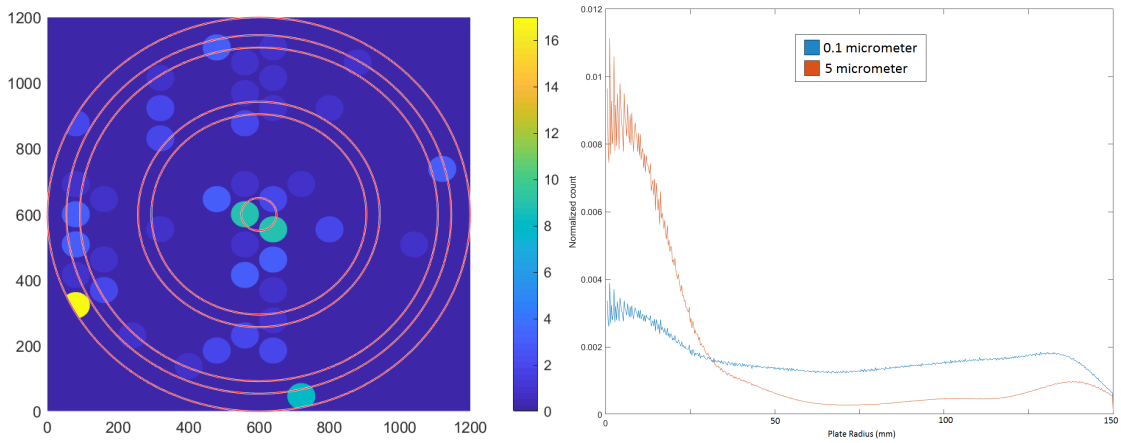

Figure 5.2: a) Heatmap (all particles counted) and b) radial graph of particle concentration on the bottom plate of the setup as a result of applying a vacuum. The blue line represents 0.1 μm particles while the orange line represents 5 μm particles.

Clearly particles in atmospheric air are able to land on the plates of the setup. This process is the same for every measurement. Hence, a share of measured particles are not a result of the experiment itself. Table 5.1 shows the amount of average particles per size bin that are a result of the measurement process per square cm.

Particle size (μm)	Amount of particles (bottom)	Amount of particles (top)
0.1	142.4	49.4
0.15	92.8	18.0
0.2	37.6	7.5
0.25	31.1	4.5
0.3	26.4	2.6
0.5	18.3	1.3
1	13.7	1.0
5	8.1	0.5

Table 5.1: Table showing amount of particles measured per square cm as a result of the measurement process (n=302). The process includes cleaning the surface with isopropyl alcohol three times, putting the plates into their positions for experiment, lowering the pressure to 1200 Pa, before repressurizing it back to atmospheric pressure.

The second part of the measurement uncertainties comes from the plotter/particle counter combination. Particles have been measured to fall from the plotter arm while moving. This was remedied by measuring away from the arm and never measure a spot where the arm has crossed over. The suction cup attachment also has a few problems. It cannot scrape over the plate because that would also release rubber from its sealing ring. An option would be to move the suction cup up while moving and down while measuring. This also proves unfeasible, as this movement also releases particles. If the suction cup does not come in contact with the plate at all, some particles might be forced off the plate in an area that is larger than the geometrical cross section of the suction cup. This causes uncertainties as it is not measurable whether a particle came from directly under the probe or from a certain distance from it. A tentative solution is to apply a Gaussian filter over the results, where it is assumed that most particles are measured directly under the probe, decaying over the width of the probe.

Another issue with the measurement technique is that the measurement probe is fairly large, so that precise location measurement is not possible and averages are used. Measurements can also influence one another if they are close enough together. The influence is an unknown quantity, and also non-measurable due to the randomness of the contamination. The individual measurement locations are therefore separated. This means that not the whole plate is measured and extrapolations and averages have to be used in order to give plausible results.

5.1.2 Flow experiment results

Before examining the effects of the plasma seal, the effects of the normal situation should be determined. In these experiments the electrodes in the setup are not powered, so that they do not create an electric field or plasma. Figure 5.3 and table 5.2 show the results of the experiments in this setting.

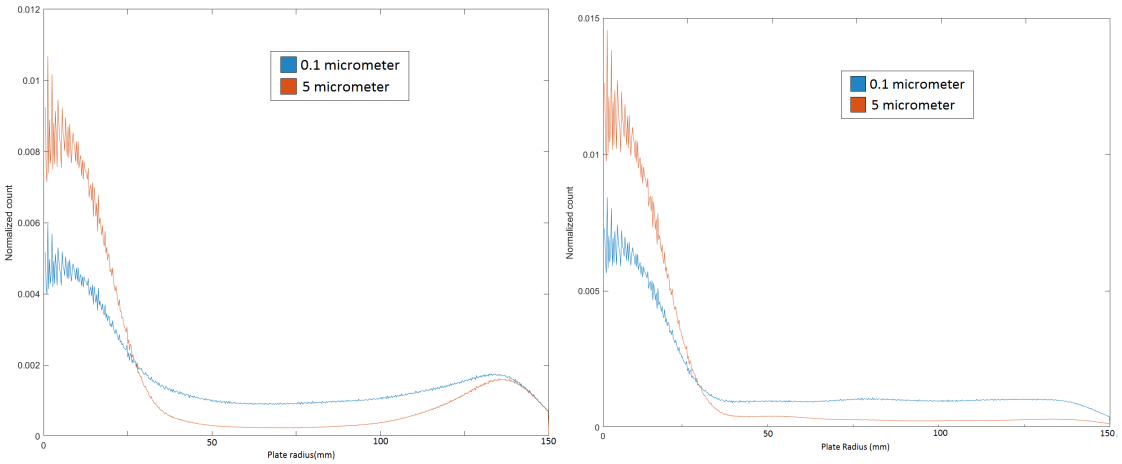

Figure 5.3: Radial particle distributions where both electrodes were not powered. a) bottom plate b) top plate

Particle size (μm)	Amount of particles (bottom)	Amount of particles (top)
0.1	213.9	70.6
0.15	153.8	18.7
0.2	62.7	7.3
0.25	53.0	5.6
0.3	44.3	4.3
0.5	30.2	2.6
1	23.4	1.9
5	16.2	1.2

Table 5.2: Table showing amount of particles measured per square cm as a result of the flow experiments using 20 shakes of the dispenser (n=302).

A number of important observations can be made from these experimental results. Firstly, from the figures the 'natural' distribution of particle end positions can be seen on the plate. A high concentration appears in the center of the bottom plate, directly underneath the dispenser. This corresponds to particles that experience next to zero radial flow in the center of the cylindrical setup. As seen in the simulations, There is a relatively constant distribution after this initial heap, followed possibly by another increase in particle concentration for larger particles. Immediately it is clear that the shape of the distribution of particles is approximately equal for both particle sizes. The difference lies in the baseline and the second heap near the edge of the plate. According to the simulations, the distribution of the smallest particles should be constant over the entire plate after the initial heap. This is not the case in the experiments. An explanation for this is that particle-particle interactions have been ignored. Clustering effects in particular cause smaller particles to follow the path of larger particles to which they are adhered. According to the specifications of the particle counter, clusters are torn apart before they are counted, which further supports this observation.

From table 5.2 and 5.1 it appears that after 20 shakes of the particle dispenser the top plate is hardly affected compared to the the control case. This agrees with the simulations as there are no upward forces near the top plate. A clear difference can be seen at the bottom plate however. In total, the amount of smallest particles increases most, while the largest particles have the highest relative increase. This means that while the particle dispenser primarily releases small particles, the most accurate results come from the larger particles.

5.2 DC results

Now the behavior of the particles in the system is known without any aid from the electrodes. Before the idea for the plasma vacuum seal is used, it is important to look at the behaviour of the particles in an electric field. This can provide useful information about the triboelectric charge on the particles and the effectiveness of the seal. For these experiments a DC voltage of 400 V was applied to the inner electrode, while the bottom plate was grounded. The outer electrode was also grounded and can be neglected.

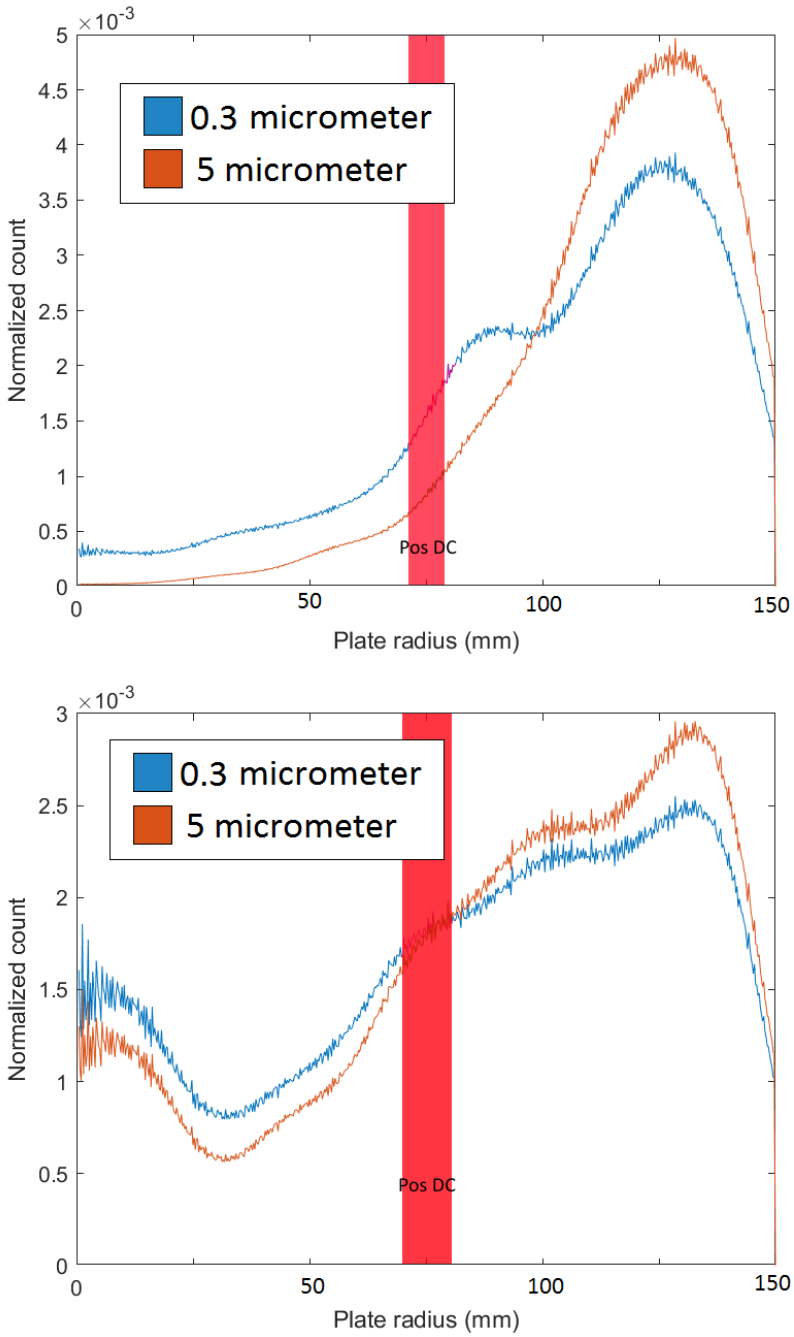

Figure 5.4: Radial particle distributions where a positive DC voltage of 400 V was applied to the inner electrode. The blue line represents 0.3 μm particles while the orange line represents 5 μm particles a) bottom plate b) top plate

It is clear from figure 5.4 that an electric field has a strong effect on both the total amount of particles and the distribution. It appears that triboelectric charge is a significant effect. Charged particles are accelerated to either the top plate if they have a negative charge or the bottom plate if they are charged positively. As there are more small particles, which are more often charged negatively, more particles will adhere to the top plate. Most of these land after they have experienced the full acceleration from the electrode (at r = 75-85 mm), as there is hardly any upward acceleration prior. The large radial spread of particles indicates a relatively high variance in negative charge.

The same experiment was repeated with a negative DC voltage. This will give information on the total distribution of charge and how particle size influences triboelectric charge. The results are shown in figure 5.5 and 5.6 below.

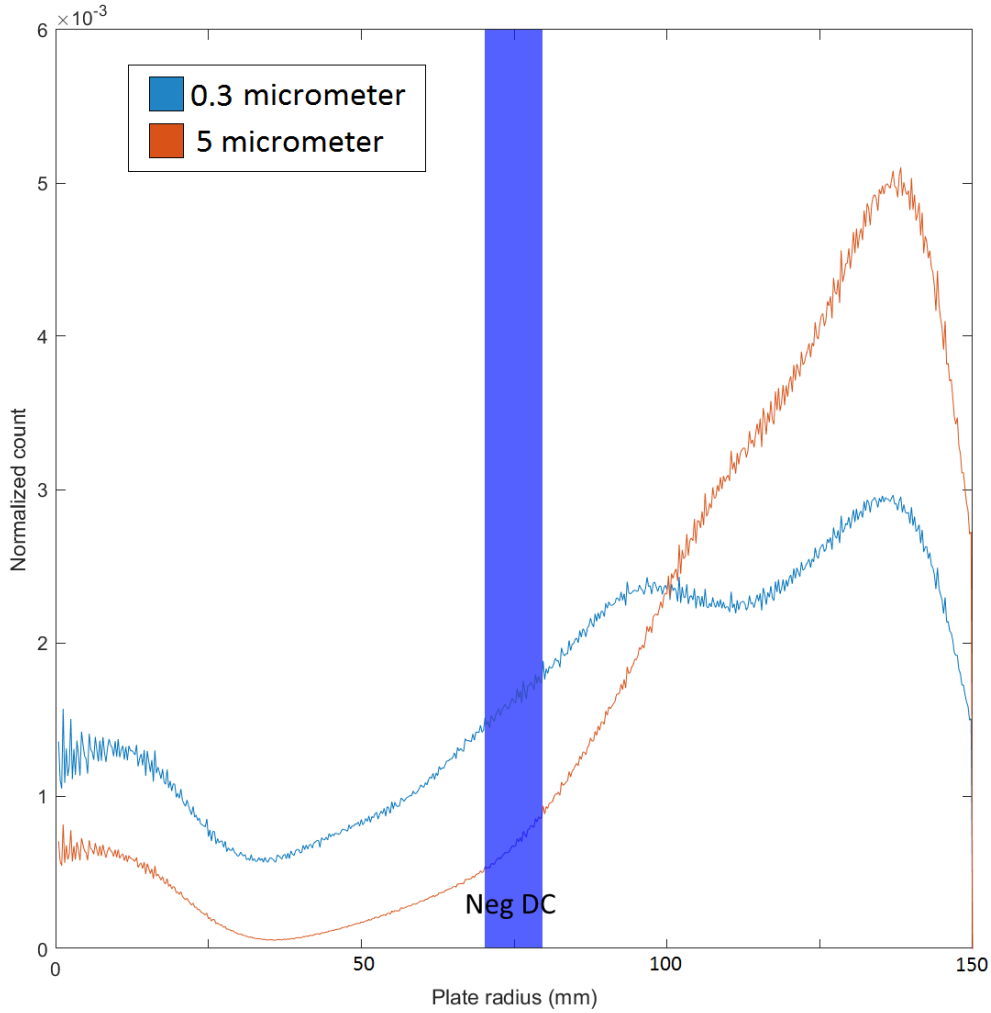

Figure 5.5: Radial particle distributions where a negative DC voltage of 400 V was applied to the inner electrode measured at the bottom plate. The blue line represents the result of the 0.3 μm particles while the orange line shows the 5 μm particles. The x-axis represents distance from the center.

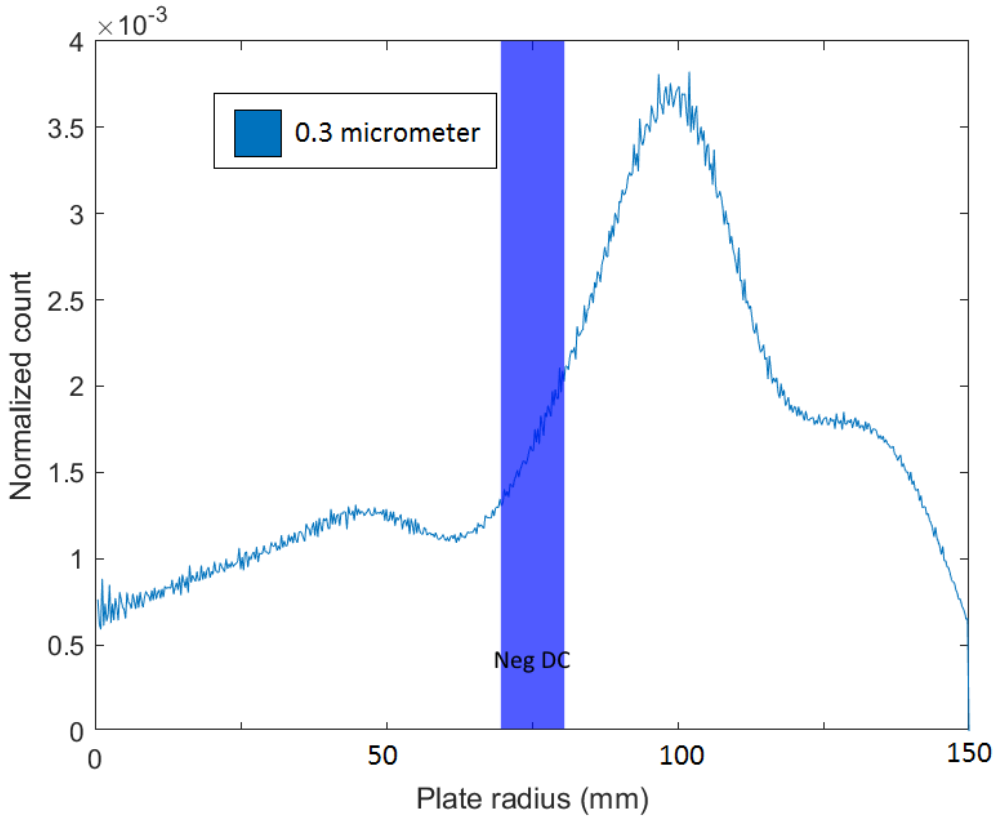

Figure 5.6: Radial particle distributions where a negative DC voltage of 400 V was applied to the inner electrode measured at the top plate. The blue line represents the result of the 0.3 μm particles while the orange line shows the 5 μm particles. The x-axis represents distance from the center.

The bottom plate, aside from minor variations, looks quite similar to the bottom plate of the positive DC result. This indicates that the charge distribution of larger particles is mostly symmetric around zero. A larger difference exists at the top plate. In the case of a negative DC voltage, there are not enough $>$ 0.3μm particles to display a reliable distribution. The distribution of the 0.3 μm particles indicates a relatively low positive charge variance, coinciding with previous studies [48]. The larger positively charged particles have very likely dropped too much in the gap to be lifted to the top by the electric field.

5.3 Plasma results

The last experiments were done while applying an AC voltage to the inner electrode, creating a plasma between the plates. The purpose is to charge the particles in a more uniform distribution to reliably alter their paths using an electric field. First the effects of the plasma itself was measured, without using the outer electrode. After this a DC voltage was applied to the outer electrode to complete the vacuum seal design. Figure 5.7 below shows the distribution of the particles after the experiment with a plasma.

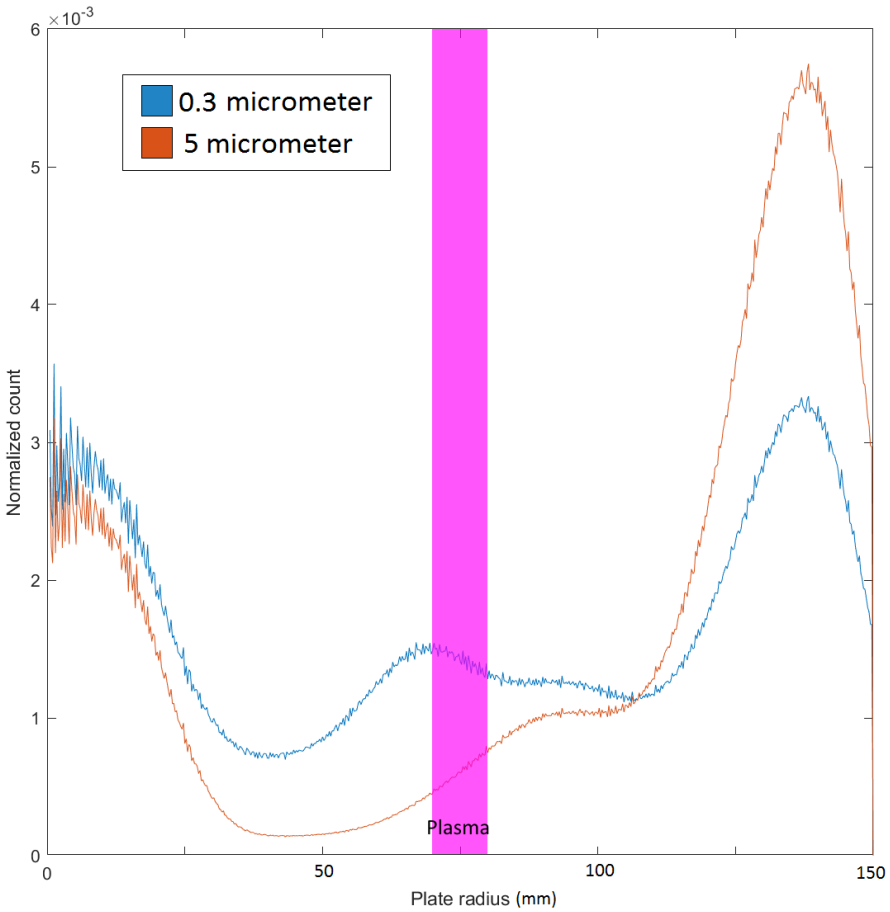

Figure 5.7: Radial particle distributions where a plasma was created underneath the inner electrode without using the outer electrode. The blue line represents the 0.3 μm particles while the orange line represents the 5 μm particles.

Clearly, particle charging is not the only important effect in the plasma. The plasma causes 3 peaks in density to appear. The first small peak is located just before the inner electrode. It can be explained by positive triboelectrically charged particles being repelled by the plasma potential before they are charged negatively by the plasma. The second peak is somewhat small and is located directly after the electrode. This increase in density may be caused by ion drag and lowly charged particles. Finally, the last and largest increase in density is located near the end of the plates. The high concentration of particles here can be caused by slow particles that leave the plasma. When these particles are highly negatively charged after entering the plasma, the radial potential gradient of the bulk edge causes these negative particles to slow down. With a slow radial velocity, the particles may settle before leaving the setup.

Also of note is that very little particles adhere to the top plate. The amount of particles is comparable to the case without use of electrodes. This is due to the small average electric field in the top part of the gap. Any potential particles that would adhere because of this field are likely charged negatively by the plasma before reaching the top.

The last experiments include the entire intended setup of the vacuum seal. This includes a plasma underneath the inner electrode and an electric field at the outer electrode. The intention is to combine the strengths of the previously examined setups. The experiments were done using either a positive or negative DC voltage of 400 V on the outer electrode. The results are shown in figures 5.8 below.

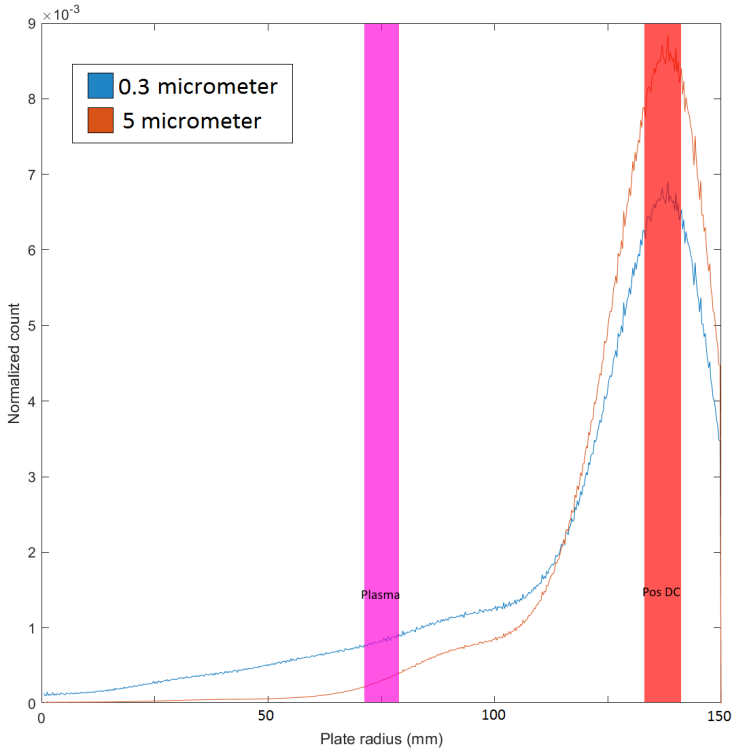

(a)

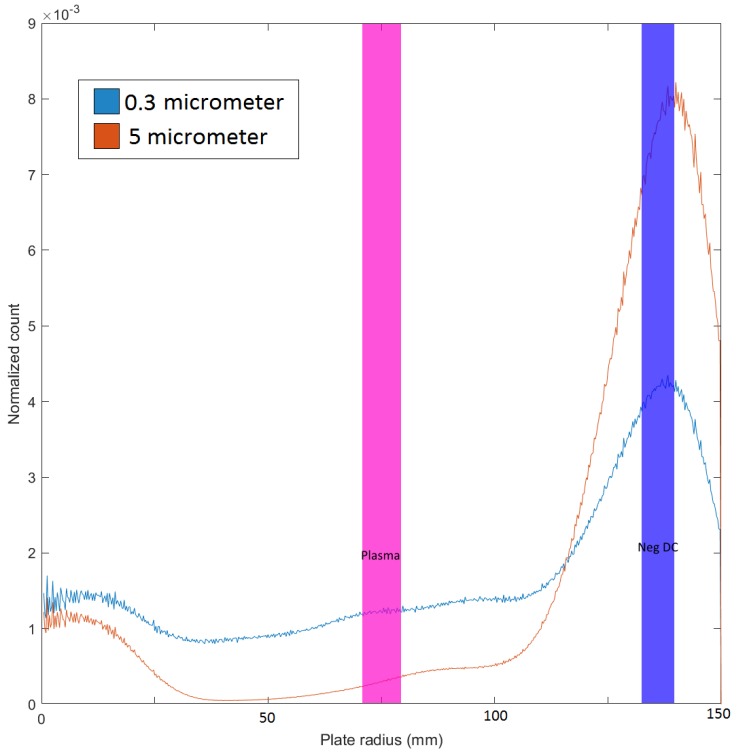

(b)

Figure 5.8: Radial particle distributions where a plasma was applied to the inner electrode and a a) positive b) negative DC voltage of 400 V was applied to the outer electrode. The blue line represents the result of the 0.3 μm particles while the orange line shows the 5 μm particles. The x-axis represents distance from the center.

These results look very similar to those of the plasma results without use of the outer electrode. The main difference is that the density increase near the outer electrode is much larger relative to the rest of the setup. This means that the setup indeed works as intended. The combined effect of the electric force and the slowing down of particles is capable of capturing many more particles than when used separately. On average this setup catches approximately twice as many particles as the setup using only one electrode. The behaviour of the particle dispenser is unfortunately too random to know what percentage of particles are contained.

5.4 Discussion

5.4.1 Flow Experiments & Simulations

The flow experiments show that most of the injected particles leave the setup without being caught by the bottom and top plate. This case shows that a vacuum seal is needed in order to avoid contamination of the wafers when being handled by the SCARA robot. The simulations are in accordance with these results. Figure 5.9 shows the comparison between the experimental results and the simulation.

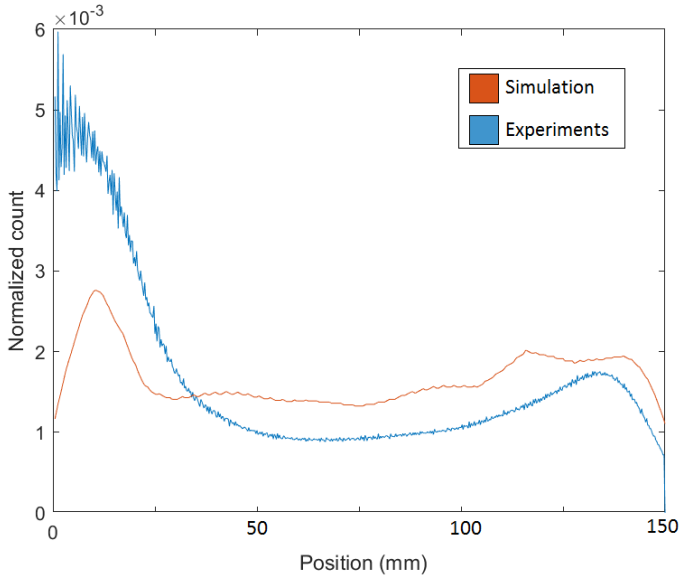

Figure 5.9: Radial particle distributions of the flow experiments and simulations for 2.5 μm particles.

These particle position distributions show that simulations can confidently be used to determine the contamination in between the plates and therefore the effectiveness of the vacuum seal. The most notable difference is the first 50 mm of the gap. Throughout the simulations proves to be a consistent distribution as this part of the gap does not change. This is caused by the assumption that the particles enter the setup evenly spread over the vertical tube. The most centrally located particles gain very little radial flow and therefore do not reach the first electrode. This causes these particles to be invariant over every simulation as this part of the gas gap does not change between simulations. The experiments show that this high particle density in the center is much smaller or even nonexistent. It can be concluded from this that the particles are not dispensed evenly. This initial condition is only important for the first 50 mm of the setup, after which the dominant effects are those of the fully evolved flow and the electrodes.

5.4.2 DC Experiments & Simulations

The addition of a DC voltage on the inner electrode was used to examine the initial charge on the particles. This charge would theoretically come from triboelectric charging, causing a net positive charge on glass particles. In general, smaller particles charge more negatively, with a wide charge distribution. Larger particles on the other hand charge more positively with a more narrow charge distribution. This information was put into the simulation as initial parameter. The initial charge distribution was then tweaked to best fit the experimental results, leading to an estimated charge of 10±40 e for 2.5 μm particles. The comparison is shown in figure 5.10 below.

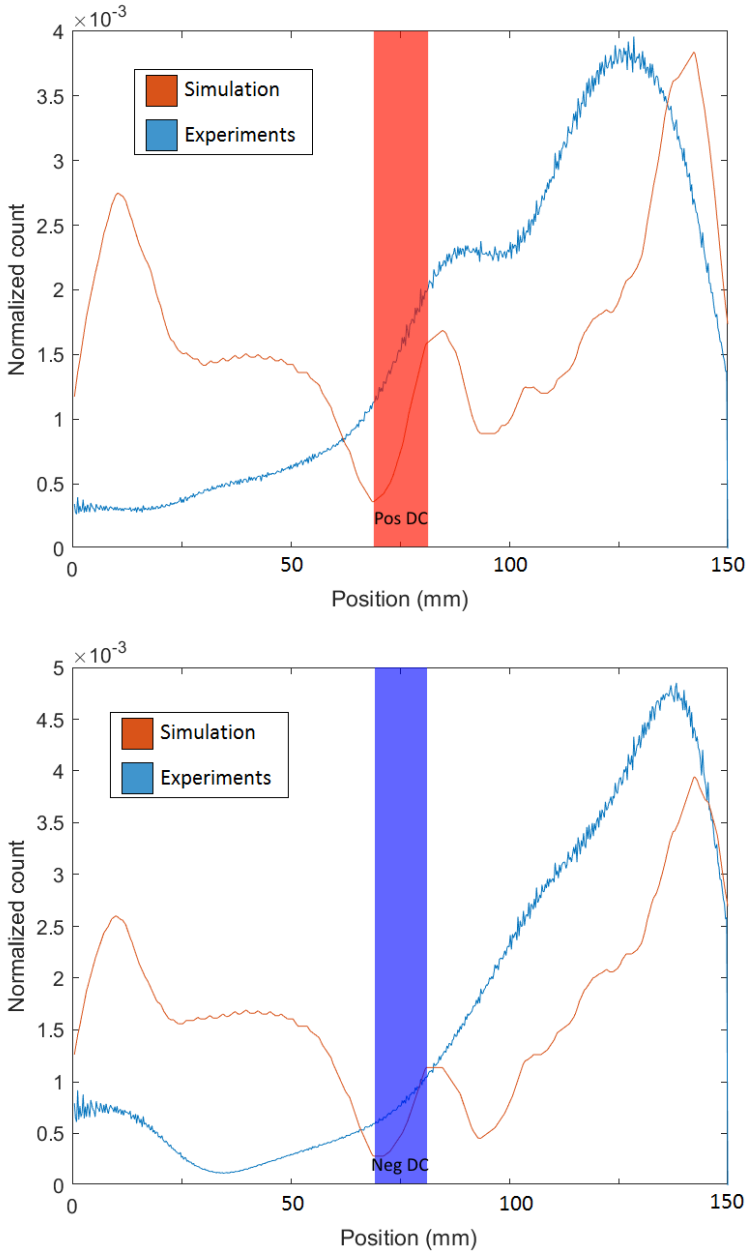

Figure 5.10: Radial particle distributions of the DC experiments and simulations for 2.5 μm particles.

5.4.3 Plasma Experiments & Simulations

Finally, a plasma was added to the setup at the inner electrode, with the option of an electric field at the outer electrode. The plasma was simulated using a 1-D model, after which the average values of the plasma potential and electron temperature were used as boundary conditions for the main model. The leftover charge after the particles leave the plasma was estimated using previous studies. The charge number was then varied to optimize the model with respect to the experimental results. The leftover charge on the particles was then chosen to be equal to -20 ± 30 e. The comparison between the experiments and simulations without use of the outer electrode is shown in figure 5.11. Figure 5.12 shows the comparison in the case for which an electric field was created at the outer electrode. Overall, the comparison between simulations and experiments are very much in agreement. Especially considering the simplicity of the plasma effects in the simulations, the results are accurate enough to predict experimental data by using simulations.

An important point to note is that the experiments and results were done at a pressure of 1200 Pa. Real life applications of the plasma seal will probably operate at even lower pressure regimes ($<$ 10 Pa). This changes a number of things, in particular the flow-induced forces and charged species density. The reduction in flow-induced forces causes a decrease in the amount of particles that escape the setup due to the lower lift force and vertical drag. From exploratory simulations, the tentative conclusion can be drawn that this effect is at least measurable. Another aspect is that Debye shielding is lessened because of the lower ion- and electron density. This will increase the effective charge on the particle, making its trajectory easier to manipulate with an electric field. The downside of a lower pressure is that it is much harder to ignite a plasma in the gas layer. A solution to this problem may be to alter the electrode placement, but this requires further research outside the scope of this thesis.

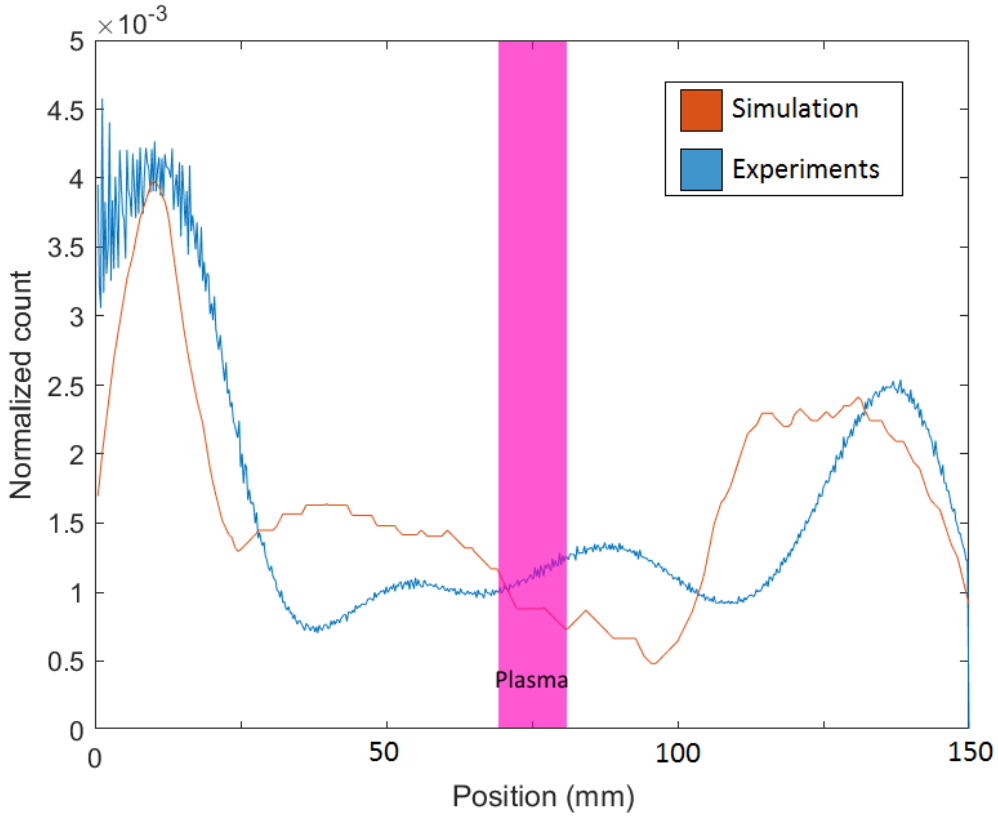

Figure 5.11: Radial particle distributions of the plasma experiments and simulations for 2.5 μm particles.

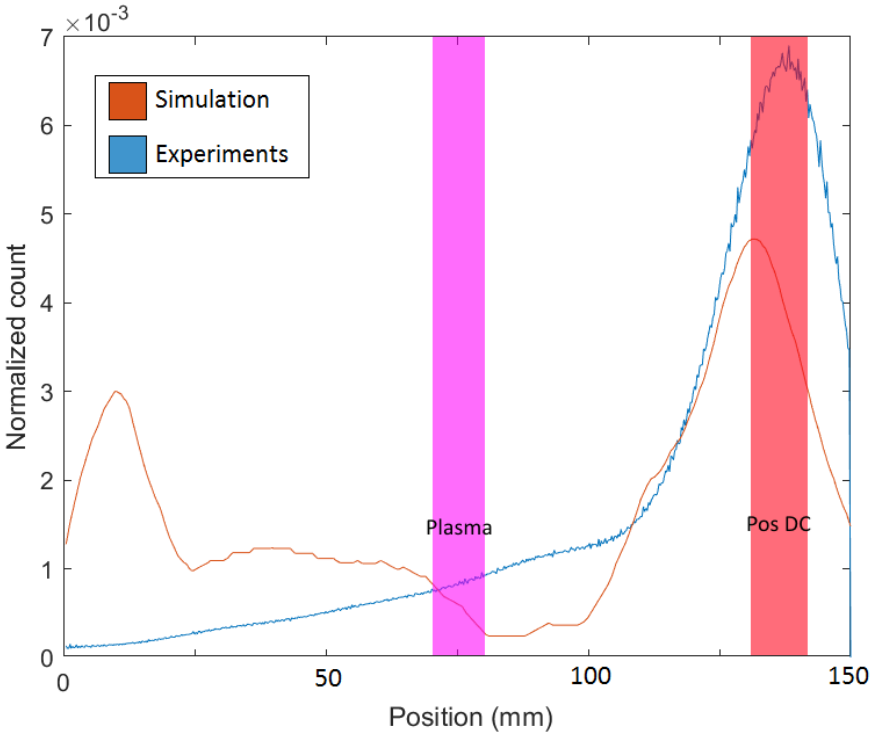

(a)

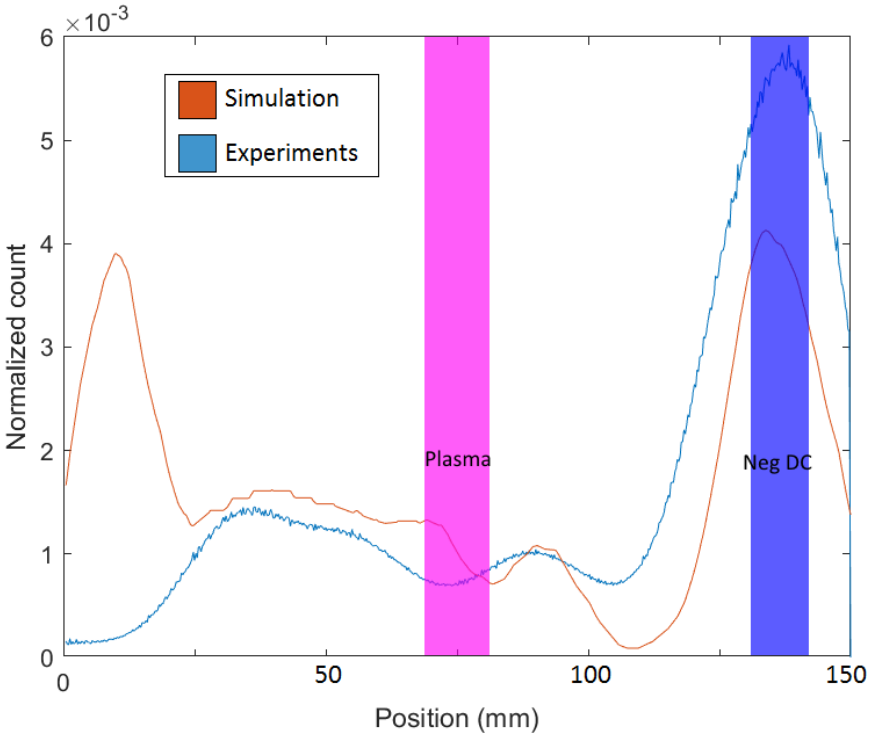

(b)

Figure 5.12: Radial particle distributions of the plasma/DC experiments and simulations for 2.5 μm particles. Applied voltage to outer electrode: a) positive 400 V b) negative 400 V.

Chapter 6

Conclusion

In this thesis, contamination by micro-particles was examined in a small gap containing radially outward flowing gas. The goal was to simulate a real-life situation of contamination from a SCARA robot in a wafer handler. Then a prototype for a vacuum seal was created to keep this contamination contained. This was done both experimentally and computationally. The design of the vacuum seal could then be optimized using a model, using the parameters that were measured and calculated from the experiments.

The experiments were done using a setup geometrically similar to that of a gas gap of a SCARA robot arm joint. Added to this were a particle dispenser and two electrodes. The injected particles serve as a measure for the trajectories and intensity of the contamination. In particular, 2.5 μm particles were examined because of low computation time for simulations and a relatively low variance in their measured position. Using a DC voltage on the inner electrode of the setup, the triboelectrically acquired initial charge on the particles was measured by comparing simulations and experiments. This charge was found to be equal to 10 ± 40 e. Apart from charge diagnostics, the DC voltage was also shown to be an effective way to contain particles.

The use of plasma in the gas gap was intended as a way to better control the particle charge. A measured effect however was an increase in measured particles around the electrode and near the edge of the bottom plate. The density increase in front of and behind the electrode is caused by positively charged particles that are repelled by the plasma potential. The largest increase in density due to the plasma can be found near the edge of the setup. This must also be caused by the plasma. The hypothesis is that particles that are charged in the plasma are slowed down by the electric field in the afterglow. Their slow radial velocity then allows the particles to settle before reaching the end of the gas gap.

The charging effect of the plasma has been estimated using OML theory. It is however unlikely that the particles reach the theoretical equilibrium charge with these experimental conditions. The charge inside the plasma is at least an order of magnitude lower than the OML predicted value of $-7*10^3$ e. After a particle leaves the plasma bulk, it is decharged in the afterglow. While the equilibrium charge remains negative, positively charged particles can also exist. To calculate the charge distribution on the 2.5 μm particles, the same idea as the DC tests was used. Again a voltage of either positive or negative 400 V was applied, this time to the outer electrode. The final charge on the particles was then used as a parameter to compare the experimental results with the simulations. The final charge on the particles was estimated to be equal to -20 ± 30 e. The sealing effect of the setup was also observed to be quite significant in these final experiments, though not fully optimized, as will be discussed in the next chapter.

Outlook

In this thesis, several conclusions have been drawn regarding the design of a plasma vacuum seal. However, this does not cover the full extent of research in this area. Some things remain unclear and require further research in order to present an optimally functioning design. This chapter will cover both those unresolved topics as well as recommendations regarding possible future exploration of the subject.

Firstly, the behaviour of particles in the experiment cannot be directly observed. Since the used setup did not allow for data gathering while the experiment was ongoing, only the end result is measured. While the simulations and theory can explain the results for the most part, direct measurement of particle trajectories is far more reliable and accurate. A modified setup that uses a high-speed camera could achieve this. To add on this, The particles that are measured are the particles that are not sucked up by the particle counter, giving an incomplete image of the contamination. Moreover, clustering has not been taken into account. Clusters can settle in the setup, acting as one larger particle with the mass of its components, but are measured as separate entities. The behaviour of singular particles can be much more easily examined when using particles of a singular size.

Another possible improvement is the measurement of charge and plasma parameters. Some of these were calculated either using theory or the simulations. Though this is inherently a good approximation for the results to be credible, more time must be taken to measure these values with greater precision to ensure greater accuracy in predicting the effects of the setup. An example would be that charging in a plasma does not occur evenly across the gap. [17]

Other possibilities for further research include optimizing the seal. While this paper explored the workings and feasibility of the vacuum seal, the design still has room for improvement. An RF plasma could be used as it lowers ion temperature, thereby increasing the maximum negative charge on the particles. The position of electrodes can be changed, for example moving the outer electrode more towards the inner electrode may prove effective in avoiding part of the decharging and/or give more room for the particles to land. Another electrode configuration consists of using a surface dielectric barrier discharge (SDBD). Smart use of the electrode positions can combine both plasma charging and flow redirection as means to provide a sealing effect [49].

Lastly, the parameters of the setup should be changed to better fit the specifications of the SCARA robot. In order to fully conclude how effective the seal can be, the real-life situation must be approached as closely as possible. For example, the dimensions of this setup do not agree with the typical SCARA robot meant to displace silicon wafers. Furthermore, the used particles are larger than encountered in those environments. The pressure is also higher than that of an actual air bearing. The used pressure in this thesis was 1200 Pa for all experiments and simulations. In the intended application the pressure is in the order of a few Pa. This will result in a much lower neutral drag and other flow-induced forces, as well as a higher plasma breakdown voltage. Simulations show that slightly fewer particles leave the setup due to the flow-induced changes, but it should be checked if this outweighs the extra difficulty of the plasma ignition.

In short, though the theory and process of the plasma vacuum seal are solid, it is still a field in which much exploration remains.

Acknowledgements

This thesis is the product of a year-long research internship, and along the way a lot of people have had an impact on it, either directly or indirectly. I could not have done this alone and I would therefore like to thank a few people in particular.

First of all I would like to thank VDL Enabling Technologies Group for making it possible for me to do this research and for their great working environment. I would like to thank Paul for his great insights in the topic and for the brainstorm-sessions that delivered most of the solutions to the obstacles along the way. I would also like to thank Job for being my contact with the university's side of things and helping me to both start and finish the project. Also a special thanks goes out to Dik, for his practical knowledge and help fixing the setup when something went wrong. Next I would like to thank Rick and Dennis for introducing me to the subject and their help getting me up to speed on the project. Also, I would like to thank Boy, Mitchel, Judith, Robert, Ilian, Luuk and Dmitri. The bi/tri-weekly meetings were of great help towards the formulation of conclusions and the measurement process.

Finally I thank my friends and family for their support, motivation and timely distractions when I needed them the most.

Appendix

6.1 Appendix A: Matlab Code

6.1.1 Plotter control

```
% port='LPT1';
% s=serial(port);
% fopen(s);
PU='echo PU > LPT1';
PD='echo PD > LPT1';
PA='echo PA > LPT1';

%positions
CENTER='echo 7500,6000 > LPT1';


%corners
C1='echo 13100,400 > LPT1';
C2='echo 1800,400 > LPT1';
C3='echo 1800,11600 > LPT1';
C4='echo 13100,11600 >LPT1';
CI1000='echo CI1000 > LPT1';

%radial
dos(PA);
xcenter=7500;
ycenter=6000;
effmaxradius=5600;
roffset=600;
maxradius=effmaxradius-roffset;
xsteps=16;
ysteps=14;
ttest=zeros([xsteps*ysteps,2]);
x=zeros(1,xsteps);
y=zeros(ysteps,xsteps);
j=1;
kvar=0.25;
for i=1:xsteps
    x(i)=xcenter-effmaxradius+(i-1)/(xsteps-1)*(2*effmaxradius);
    for k=1:ysteps
        yc=ycenter-effmaxradius+(k+kvar-1.25)/(ysteps-1)*(2*effmaxradius);
        if (x(i)-xcenter)^2+(yc-ycenter)^2+1<=(effmaxradius)^2
            y(j,i)=yc;
            j=j+1;
        end
    end
    kvar=-kvar;
    j=1;
end
disp('calc done')
pause(1);
dos('echo 13100,3415 > LPT1');
pause(3);
measuretime=11;
```

```
correctiontime=0.85; %Also don't change
totaltime=measuretime+correctiontime+0.15;
tic
pause(correctiontime);
i=1;
revpar=-1;
for j=1:xsteps
    for k=1:ysteps
       % i=phisteps*(r-1)+phi;
       if y((ysteps+1)*sign(-revpar+1)+sign(revpar)*k,j)>0
        dos(['echo ',num2str(x(xsteps+1-j)),', ',num2str(y((ysteps+1)*sign(-revpar
    +1)+sign(revpar)*k,j)),' > LPT1']);
        pause(measuretime);
        ttest(i,[1,2])=[toc/i-totaltime,totaltime*i];
        pause(correctiontime-i*ttest(i,1))
        i=i+1;
       end
    end
    revpar=-revpar;
    disp([num2str(i-1),' out of ', num2str(length(y(y>0)))]);
end
tetetttest=ttest(:,1)+totaltime;
tonk(:,[1,2,3])=[tetetttest(:,1).*ttest(:,2)/totaltime,ttest(:,2),tetetttest(:,1).*
    ttest(:,2)/totaltime-ttest(:,2)];
dos('echo 15000,400 > LPT1');
```

6.1.2 Particle counter read

```
A=readmatrix('C:\Users\s145512\Desktop\particlecounter\newDCalu.xlsx');%-readmatrix
    ('C:\Users\s145512\Desktop\particlecounter\newflowalu.xlsx');
%A(246,:)=0;
% column=5; % 5<=integer<=12 or series like 5:12
xsteps=16;
ysteps=14;
rrrr=zeros(600,8);
psize=1200;
xcenter=7500;
ycenter=6000;
effmaxradius=5600;
roffset=600;
for column=5:10
q=2;
j=1;
kvar=0.25;
x=zeros(1,xsteps);
y=zeros(ysteps,xsteps);



    B=zeros(ysteps,xsteps);
for i=1:xsteps
    x(i)=xcenter-effmaxradius+(i-1)/(xsteps-1)*(2*effmaxradius);
    for k=1:ysteps
        yc=ycenter-effmaxradius+(k+kvar-1.25)/(ysteps-1)*(2*effmaxradius);
        if (x(i)-xcenter)^2+(yc-ycenter)^2+1<=(effmaxradius)^2
            B(j,i)=sum(A(q,column));
            y(j,i)=yc;
            j=j+1;
            q=q+1;
        end
    end
    kvar=-kvar;
    j=1;
end
if column>=1
C=zeros(psize);
D=C;
for k=1:xsteps
    for j=1:ysteps
```

```
        xmeas=round(psize/2+(x(k)-xcenter)/effmaxradius*psize/2);
        ymeas=round(psize/2+(y(j,k)-ycenter)/effmaxradius*psize/2);
        if ymeas>0
        if xmeas>0
        for measurex=-psize/30:psize/30
            for measurey=-psize/30:psize/30
                if measurex^2+measurey^2<=(psize/30)^2 && (measurex+xmeas-psize/2)^2+(measurey+ymeas-psize/2)^2<=(psize/2)^2
                    D(xmeas+measurex,ymeas+measurey)=1;
                    if C(xmeas+measurex,ymeas+measurey)==0
                        C(xmeas+measurex,ymeas+measurey)=C(xmeas+measurex,ymeas+measurey)+B(j,k);
                    else
                        C(xmeas+measurex,ymeas+measurey)=C(xmeas+measurex,ymeas+measurey)+0.3*normpdf(measurex^2+measurey^2,0,2000)*B(j,k);
                    end
                    %C(xmeas+measurex,ymeas+measurey)=C(xmeas+measurex,ymeas+measurey)+normpdf(measurex^2+measurey^2,0,2000)*B(k,j);
                end
            end
        end
        end
        end
    end
end
Cblur=imgaussfilt(10*C,30);
for i=1:1200
for j=1:1200
if round(sqrt((abs(psize/2-i))^2+(abs(psize/2-j))^2),0)+1<psize/2
rrrr(round(sqrt((abs(psize/2-i))^2+(abs(psize/2-j))^2),0)+1,column-4)=rrrr(round(sqrt((abs(psize/2-i))^2+(abs(psize/2-j))^2),0)+1,column-4)+Cblur(i,j)/sqrt((abs(psize/2-i))^2+(abs(psize/2-j))^2);
end
end
end
end
    disp([num2str(column)-4, ' out of 8'])
end
centers=psize/2*[1 1; 1 1; 1 1; 1 1; 1 1; 1 1];
radii=psize/30*[1.25 7.625 8.575 12.7 13.65 15];
imshow(Cblur,[]);
%s=surf(Cblur);
colorbar
%s.EdgeColor='none';
viscircles(centers,radii,'linewidth',0.1)



%plot(rrrr)
plot([2:600],(rrrr([2:600],1)/sum((rrrr([2:600],1)))),[2:600],(rrrr([2:600],5)/sum((rrrr([2:600],5)))))
xlabel('Plate radius (mm)')
ylabel('Normalized count')
print -clipboard -dbitmap
```

Bibliography

[1] G.E. Moore. Cramming more components onto integrated circuits, reprinted from electronics. *Electronics*, 38(8), 2005.

[2] P. Blom J. Beckers, B. van Minderhout. Particle contamination control by application of plasma. In Nelson M. Felix and Anna Lio, editors, *Extreme Ultraviolet (EUV) Lithography XI*, volume 11323, pages 558 – 563. International Society for Optics and Photonics, SPIE, 2020.

[3] B. van Minderhout. The charge of micro-particles in a low pressure spatial plasma afterglow. *Journal of Physics D: Applied Physics*, 52(32), 2019.

[4] B. Platier. Resonant microwaves probing the spatial afterglow of an rf plasma jet. *Appl. Phys. Lett.*, 115, 2019.

[5] R. J. M. M. Snijkers. *The sheath of an RF plasma : measurements and simulations of the ion energy distribution*. PhD thesis, Technische Universiteit Eindhoven, 1993.

[6] M. K. Zuraw D. M. Dobkin. *Principles of Chemical Vapor Deposition*. Springer Netherlands, 2003.

[7] R. Brandenburg. Dielectric barrier discharges: progress on plasma sources and on the understanding of regimes and single filaments. *Plasma Sources Science and Technology*, 26(5):053001, 2017.

[8] E. Wagenaars. *Plasma breakdown of low-pressure gas discharges*. PhD thesis, Department of Applied Physics, 2006.

[9] J. A. L. Schmeltekopf, H. P. Broida. Short-duration visible afterglow in helium. *The Journal of Chemical Physics*, 1963.

[10] L. Couedel. Influence of the ambipolar-to-free diffusion transition on dust particle charge in a complex plasma afterglow. *Physics of Plasmas*, 15(6), 2008.

[11] B. van Minderhout. The dynamics of particles in plasma (afterglow). Master's thesis, Department of Applied Physics, 2016.

[12] XZ. Tang G. L. Delzanno. Comparison of dust charging between orbital-motion-limited theory and particle-in-cell simulations. *Physics of Plasmas*, 2015.

[13] X. Tang. Orbital-motion-limited theory of dust charging and plasma response. *Physics of Plasmas*, 21, 2014.

[14] M.J.M. Parrot. Theory of cylindrical and spherical langmuir probes in the limit of vanishing debye number. *The Physics of Fluids*, 25, 1982.

[15] J.G. Laframboise. Theory of spherical and cylindrical langmuir probes in a collisionless, maxwellian plasma at rest. *Aerospace Engineering Reports*, UTIAS Report, No. 100, 1966.

[16] S. Ratynskaia. Experimental determination of dust-particle charge in a discharge plasma at elevated pressures. *Physical Review Letters*, 93(8), 2004.

[17] L. Matthews A. Douglass, V. Land. Dust particle charge in plasma with ion flow and electron depletion near plasma boundaries. *Physics of Plasmas*, 18(8):083706, 2011.

[18] M. Russell T. Matsoukas. Particle charging in low-pressure plasmas. *Journal of Applied Physics*, 1995.

[19] L. Couedel. Residual dust charges in discharge afterglow. *Phys. Rev. E*, 74(2), 2006.

[20] M. Mikikian L. Couedel, A. Samarian. Dust charge distribution in complex plasma afterglow. *EPL (Europhysics Letters)*, 84:35002, 10 2008.

[21] A. Samarian L. Couëdel, A. Mezeghrane. Complex plasma afterglow. *Contributions to Plasma Physics*, 49(4-5):235–259, 2009.

[22] A. A. Mamun P. K. Shukla. Introduction to dusty plasma physics. *Plasma Physics and Controlled Fusion*, 2002.

[23] Paul S. Epstein. On the resistance experienced by spheres in their motion through gases. *Phys. Rev.*, 1924.

[24] H. Wang Z. Li. Drag force, diffusion coefficient, and electric mobility of small particles. *Soft Matter Phys.*, 2003.

[25] J. Pelletier. *Dusty Plasmas: Physics, Chemistry and Technological Impacts in Plasma Processing*. Wiley, 2000.

[26] W. J. Goedheer. V. Land. Manipulating dust charge using ultraviolet light in a complex plasma. *IEEE Transactions on plasma science*, 2007.

[27] J. Beckers. *Dust particle(s) (as) diagnostics in plasmas*. PhD thesis, Department of Applied Physics, 2011.

[28] J. C. Forster M.S. Barnes, J.H. Keller. Transport of dust particles in glow-discharge plasmas. *Phys. Rev. E*, 68(3), 1992.

[29] H M Thomas, G E Morfill, V E Fortov, A V Ivlev, V I Molotkov, A M Lipaev, T Hagl, H Rothermel, S A Khrapak, R K Suetterlin, M Rubin-Zuzic, O F Petrov, V I Tokarev, and S K Krikalev. Complex plasma laboratory PK-3 plus on the international space station. *New Journal of Physics*, 2008.

[30] V.E. Fortov, A.V. Ivlev, S.A. Khrapak, A.G. Khrapak, and G.E. Morfill. Complex (dusty) plasmas: Current status, open issues, perspectives. *Physics Reports*, 2005.

[31] R.W. Schefer L. Talbot, R.K. Cheng. Thermophoresis of particles in a heated boundary layer. *Journal of Fluid Mechanics*, 101(4), 1980.

[32] J. Dejeu M. Gauthier, S. Alvo. Analysis and specificities of adhesive forces between microscale and nanoscale. *IEEE Transactions on Automation Science and Engineering*, 10(3):562–570, 2013.

[33] H.C. Hamaker. The london—van der waals attraction between spherical particles. *Physica*, 1937.

[34] L.C.J. Heijmans. *Quantifying plasma particle lofting*. PhD thesis, Department of Applied Physics, 2017. Proefschrift.

[35] J. Peters. Implementing the lofting force to remove particles from wafers. Master's thesis, Department of Applied Physics, 2018. Masters Thesis.

[36] A.L. London R.K. Shah. *Laminar flow forced convection in ducts : a source book for compact heat exchanger analytical data*. Academic Press, 1978.

[37] J. Cimbala Y. Cengel. *Fluid mechanics : fundamentals and applications.* Mcgraw-Hill Education - Europe, 2013.

[38] A. Stickland N. Ekanayake, J. Berry. Lift and drag forces on a particle near a wall at low reynolds numbers. 12 2018.

[39] Jun Zhang, Weihua Li, and Gursel Alici. *Inertial Microfluidics: Mechanisms and Applications*, pages 563–593. 10 2017.

[40] Paul Fischer L. Zeng, S. Balachandar. Wall-induced forces on a rigid sphere at finite reynolds number. *Journal of Fluid Mechanics*, 536, 2005.

[41] S. Balachandar L. Zeng, F. Najjar. Forces on a finite-sized particle located close to a wall in a linear shear flow. *Phys. Fluids*, 21, 2009.

[42] Seyed Hamid Tabaeikazerooni. Laminar and turbulent particle laden flows : a numerical and experimental study. 2019.

[43] D.J. Lacks K.M. Forward. Particle-size dependent bipolar charging of martian regolith simulant. *Geophysical Research Letters*, 36(13), 2009.

[44] L. C. J. Heijmans and S. Nijdam. Triboelectric and plasma charging of microparticles. *EPL (Europhysics Letters)*, 114(6), 2016.

[45] M.S. Abd-Elhady, C.C.M. Rindt, J.G. Wijers, and A.A. van Steenhoven. Modelling the impaction of a micron particle with a powdery layer. *Powder Technology*, 168(3):111 – 124, 2006.

[46] S. Nijdam L.C.J. Heijmans. Triboelectric and plasma charging of microparticles. *Europhysics Letters*, 114(6), 2016.

[47] A. Levandovsky D.J. Lacks. Effect of particle size distribution on the polarity of triboelectric charging in granular insulator systems. *Journal of Electrostatics*, 65(2), 2007.

[48] V. Lee J.M. Pierson S.R. Waitukaitis. Size-dependent same-material tribocharging in insulating grains. *Phys. Rev. Lett.*, 112:218001, 2014.

[49] L.Veldhuis M. Kotsonis, S. Ghaemi. Measurement of the body force field of plasma actuators. *Journal of Physics D: Applied Physics*, 44, 01 2011.